

Cooling through quantum criticality and many-body effects in condensed matter and cold gases

Bernd Wolf

*Institute of Physics, Goethe Universität, SFB/TR 49
Max-von-Laue Strasse 1, 60438 Frankfurt, Germany
wolf@physik.uni-frankfurt.de*

Andreas Honecker*

*Institute for Theoretical Physics, Georg-August-Universität Göttingen
Friedrich-Hund-Platz 1, 37077 Göttingen, Germany
honecker@theorie.physik.uni-goettingen.de*

Walter Hofstetter

*Institute for Theoretical Physics, Goethe Universität, SFB/TR 49
Max-von-Laue Strasse 1, 60438 Frankfurt, Germany
hofstett@physik.uni-frankfurt.de*

Ulrich Tutsch

*Institute of Physics, Goethe Universität, SFB/TR 49
Max-von-Laue Strasse 1, 60438 Frankfurt, Germany
tutsch@physik.uni-frankfurt.de*

Michael Lang

*Institute of Physics, Goethe Universität, SFB/TR 49
Max-von-Laue Strasse 1, 60438 Frankfurt, Germany
Michael.Lang@physik.uni-frankfurt.de*

Received 29 August 2014

Accepted 7 September 2014

Published 10 October 2014

This article reviews some recent developments for new cooling technologies in the fields of condensed matter physics and cold gases, both from an experimental and theoretical point of view. The main idea is to make use of distinct many-body interactions of the system to be cooled which can be some cooling stage or the material of interest itself, as is the case in cold gases. For condensed matter systems, we discuss magnetic cooling schemes based on a large magnetocaloric effect as a result of a nearby quantum phase transition and consider effects of geometrical frustration. For ultracold gases, we review many-body cooling techniques, such as spin-gradient and Pomeranchuk cooling, which can be applied in the presence of an optical lattice. We compare the cooling performance of these new techniques with that of conventional approaches and discuss state-of-the-art applications.

Keywords: magnetic cooling; correlated electron systems; ultracold gases.

*Address after September 1, 2014: Laboratoire de Physique Théorique et Modélisation, Université de Cergy-Pontoise, 2 avenue A. Chauvin, 95302 Cergy-Pontoise cedex, France.

1. Introduction

The properties of matter at low temperatures continue to be of high interest. Phenomena such as novel types of superconductivity/superfluidity, quantum phase transitions or different types of topological order fascinate a growing community of researchers. Advancements in these different areas rely on suitable coolants. Since standard cooling technologies, used in experiments on condensed matter systems, are based on ^3He which is difficult in handling and of limited availability, alternative cooling technologies are required. Likewise, with the advent of ultracold gases as tunable quantum simulators for the above-mentioned many-body effects, there is an increasing demand for efficient cooling technologies in this rapidly developing field.

For experiments on **condensed matter systems**, P. Debye¹ and W. F. Giauque² independently suggested in 1926 to use the magnetocaloric effect (MCE) of paramagnetic materials to reach temperatures significantly below 1 K. This effect, which describes temperature changes of a magnetic material in response to an adiabatic change of the magnetic field, forms the basis of magnetic refrigeration with the main area of applications focussing on cryogenic temperatures.^{3,4,5} A highly topical area of research has been triggered by the observation of a giant MCE around room temperature.⁶ This discovery has stimulated additional work^{7,8} indicating the potential of the MCE for an environment-friendly room-temperature refrigeration.

A large MCE, and with it a large cooling effect, can be expected for materials where the entropy S strongly changes with the magnetic field B . This is the case for paramagnetic salts, the materials of choice for low-temperature refrigeration.³ These systems are characterized by a three-dimensional (3D) array of spin-carrying centres, with a sufficiently large inter-site distance so that residual magnetic interactions are weak. Besides their large $\partial S/\partial B$ values, paramagnets excel by their ease of operation as compared to ^3He - ^4He dilution refrigerators, the standard cooling technology for reaching sub-Kelvin temperatures. In addition, paramagnets can be operated under microgravity conditions, where standard dilution refrigerators fail, and are thus vital in present space applications.^{9,10}

An extension of the concept of paramagnets includes molecular nanomagnets, where the magnetic centres consist of extended, magnetically isolated molecules. Recently it has been recognized that these systems can exhibit a large MCE at low temperatures which makes them attractive for magnetic cooling.^{11,12} High-spin single molecules with a large spin value (superparamagnets), having a small or vanishing anisotropy, are particularly favourable. The reason for that is the large corresponding magnetic entropy of these molecules which can be easily polarized in a magnetic field.¹³ Some of the superparamagnets are also geometrically frustrated and therefore exhibit large changes of their magnetization below the saturation field, in favour of a large MCE.^{14,15}

An alternative to the above paramagnetic systems is provided by geometrically frustrated magnets,^{16,17,18,19,20} characterized by considerable inter-site magnetic interactions which compete with each other. Starting with the recognition that the

magnetocaloric substance $\text{Gd}_3\text{Ga}_5\text{O}_{12}$ ^{21,22,23,24} owes its large MCE to geometric frustration, experimental and theoretical studies have established these systems as powerful coolants for temperatures in the Kelvin range with a minimum accessible temperature around 0.5 K. Despite the interaction between neighbouring spins, strongly frustrated magnets remain in a so-called disordered cooperative paramagnetic state with finite entropy at temperatures well below the materials' Curie-Weiss temperatures.²⁵ In this temperature range and under suitable conditions the cooling rate $(\partial T/\partial B)_S$ for classical spin systems can exceed the values obtained for paramagnets by more than one order of magnitude.²⁶ The enhanced cooling rate of geometrically frustrated magnets in the cooperative paramagnetic state is due to the magnetic entropy which results from a macroscopic number of local modes that at the classical level remain gapless up to the saturation field.²⁷ In contrast, for non- or weakly-frustrated antiferromagnets, the condensation of only one or a few modes leads to long-range order described by a certain wave vector.²⁶ Remarkably, due to exact “localized magnon” states,^{28,29,30,31,32,33} the classical degeneracy and thus the good magnetocaloric properties survive quantum fluctuations at the saturation field.

The well-established “classical” cooling systems mentioned further above have been extensively discussed in the literature and there are numerous excellent review articles available, see, e.g., Refs. 7,34,35. In the present paper we focus on an alternative Ansatz taken up more recently. Here a strongly field-dependent entropy, and with it a large MCE, is the result of distinct many-body interactions. These are materials close to a quantum-critical point (QCP) – a zero-temperature phase transition – separating an ordered from a quantum-disordered state. For these materials the low-temperature properties are governed by strong quantum many-body effects which give rise to a peculiar entropy landscape. The transition to saturation in highly frustrated magnets mentioned before can be considered as one example for this category. These new coolants may provide a useful alternative for experiments in the sub-Kelvin temperature range where they have the potential to replace established cooling technologies based on ^3He .

In **ultracold gases**, a major current challenge is reaching the low temperatures (entropies) required for observing solid-state type ordered states, for example quantum magnetism induced by superexchange, or d -wave superfluidity, which would allow highly tunable quantum simulations of model systems such as the fermionic Hubbard model^{36,37} or Heisenberg spin models. While Mott-insulating phases^{38,39} short-range magnetic correlations⁴⁰ and tunable magnetic exchange couplings⁴¹ have already been realized both in bosonic and fermionic multiflavor gases, true long-range magnetic order in optical lattices has so far only been observed in a realization of the quantum XY model via a tilted bosonic Mott-insulator, where the effective magnetic exchange is linear in the hopping amplitude instead of quadratic⁴². Current estimates of entropies per particle in a fermionic ^4He Mott insulator yield $S/N \approx k_B \ln 2$, which is roughly twice the critical entropy for Néel ordering⁴³.

In order to reach these low temperatures (entropies), new cooling techniques in the presence of an optical lattice need to be implemented. In contrast to solid-state materials, ensembles of ultracold gases in optical lattices are to a very good approximation closed quantum systems, where the total entropy remains constant if the time evolution, e.g., during a lattice ramp, is adiabatic. The quantum phases under investigation, such as Mott insulator or magnetic states, are therefore uniquely characterized by their entropies per particle, while the corresponding temperatures depend on the strength of the optical lattice potential and on the atomic scattering properties, and are non-universal. In the following discussion we will, for this reason, mostly focus on entropy instead of temperature.

The goal is then to either prepare a sufficiently low-entropy initial state, which upon (approximately) adiabatic ramp-up of the lattice becomes magnetically ordered, or to separate entropy-rich from low-entropy regions of the sample, e.g., by shaping the optical potential or by magnetic gradients. Both approaches will be discussed in section 3.2.

The paper is organized as follows. After describing the basic thermodynamic relations for magnetic cooling in section 2, we discuss in section 3 different concepts by comparing the conventional approach for magnetic cooling with the novel Ansatz of cooling through many-body effects. Section 3.3.3 deals with the magnetic cooling of real systems before typical applications are discussed in section 4.

2. Basic relations

We start by reviewing some basic properties of the magnetocaloric effect. For simplicity, we focus on a purely magnetic system that can be described by a free energy $F(T, B, N)$ where T is the temperature, B the external magnetic field and N the number of spins (particles). In canonical thermodynamics the free energy is expressed via the partition function Z as $F = -k_B T \ln Z$. This is of course a very useful relation in order to compute the thermodynamic quantities for a given model, but in this section we rather want to recall that some useful results can already be derived on general grounds.

The physical quantities of interest are obtained by appropriate partial derivatives of the free energy, in particular the *entropy*

$$S = -\frac{\partial F}{\partial T}, \quad (1)$$

the *magnetization*

$$M = -\frac{\partial F}{\partial B}, \quad (2)$$

and the *specific heat*

$$C = T \frac{\partial S}{\partial T}. \quad (3)$$

This last relation is already useful for analysing experiments since it allows one to reconstruct the experimentally inaccessible entropy from the experimentally accessible specific heat ⁴ in the form $\Delta S = \int \frac{C}{T} dT$.

Now let us consider a change in an external magnetic field B . In general, the system will respond with a change of temperature T . The *magnetocaloric effect* is defined as the corresponding derivative $\partial T / \partial B$. If we consider perfectly adiabatic conditions, i.e., constant entropy S , we can capture this effect by introducing a *magnetic Grüneisen parameter*

$$\Gamma_B := \frac{1}{T} \left(\frac{\partial T}{\partial B} \right)_S. \quad (4)$$

By virtue of Eq. (1), the entropy is also a function of T , B , and N . Keeping N fixed, and using Eq. (3) we have

$$dS = \frac{\partial S}{\partial T} dT + \frac{\partial S}{\partial B} dB = \frac{C}{T} dT + \frac{\partial S}{\partial B} dB. \quad (5)$$

Under adiabatic conditions we have $dS = 0$, thus

$$0 = \frac{C}{T} \left(\frac{\partial T}{\partial B} \right)_S + \left(\frac{\partial S}{\partial B} \right)_T, \quad (6)$$

and hence with Eq. (4)

$$\Gamma_B = -\frac{1}{C} \left(\frac{\partial S}{\partial B} \right)_T = -\frac{(\partial S / \partial B)_T}{T (\partial S / \partial T)_B}. \quad (7)$$

The analogy of the last form to a similar expression for the classical, *thermal Grüneisen parameter* used in describing the thermal expansion, motivates the name as well as the inclusion of the factor $1/T$ into the definition (4). ^{44,45}

Finally, the derivative of the entropy with respect to magnetic field can be eliminated using the definitions Eqs. (1) and (2) and one finds

$$\Gamma_B = -\frac{1}{C} \frac{\partial M}{\partial T}. \quad (8)$$

This relation has been widely used experimentally since it relates the magnetocaloric effect to the specific heat and the variation of magnetization with temperature at a given temperature, i.e., quantities that are straightforward to measure without the need to ensure adiabatic conditions.

As a first simple application let us consider an *ideal paramagnet* that we may characterize by an entropy that is a function of only the ratio B/T but not of both parameters individually, i.e., $S = S(B/T, N)$. It follows that $C = -B \frac{\partial S}{\partial B}$ and thus with Eq. (7)

$$\Gamma_B = \frac{1}{B} \quad (9)$$

for an ideal paramagnet. Actually, given that $S = S(B/T, N)$, the temperature T has to vary linearly with magnetic field B in order to keep the entropy constant.

Thus, for an ideal paramagnet $\partial T/\partial B$ has to be constant along an adiabatic demagnetization curve which is a straight line going to zero for $B \rightarrow 0$. The slope of the line through $(0, 0)$ and (T, B) is $\frac{T}{B}$, i.e., $(\frac{\partial T}{\partial B})_S = \frac{T}{B}$. Upon division by T , one recovers Eq. (9) from these basic considerations.

The behaviour of the *magnetic Grüneisen parameter* in the vicinity of a *quantum critical point* – a zero-temperature phase transition – is a bit more involved, but some conclusions can already be reached with the tools above and simple scaling assumptions.^{44,45} Let us consider a field-induced quantum phase transition at $B = B_c$, i.e., a transition between two distinct phases that meet at $B = B_c$ for $T = 0$. Introducing the scaling parameter

$$r = \frac{B - B_c}{B_0} \quad (10)$$

with some field scale B_0 , the singular part of the free energy density close to a second-order quantum phase transition can be cast in the scaling form⁴⁵

$$f(B, T) = a^{-(d+z)} g(r a^{1/\nu}, T a^z) \quad (11)$$

with d the spatial dimension, z the dynamical critical exponent, ν the correlation length critical exponent, and g a scaling function. Firstly, we can choose the arbitrary scale parameter $a = r^{-\nu}$ in order to find

$$f(B, T) = r^{(d+z)\nu} g(1, T r^{-z\nu}) =: r^{(d+z)\nu} \tilde{g}(T r^{-z\nu}), \quad (12)$$

where \tilde{g} is a new one-parameter scaling function. If we are interested in the low-temperature limit $T \rightarrow 0$, $r \neq 0$, we can set $x = T r^{-z\nu}$ and expand⁴⁴

$$\tilde{g}(x) = \tilde{g}(0) + C x^{y_0+1} + \dots, \quad (13)$$

where y_0 is another exponent whose value may depend on the side of the phase transition, i.e., the value of y_0 may be different for $r < 0$ and $r > 0$.

Now it remains to analyse the derivatives of the free energy using the scaling form Eq. (12) and the expansion (13).^{44,45} First, one observes that the entropy density $S/V = -\partial f/\partial T$ scales as $S/V \propto T^{y_0}$, i.e., $y_0 > 0$ is required in order to satisfy the third law of thermodynamics. Finally, considering second derivatives and using Eq. (7) one finds the scaling form of the magnetic Grüneisen parameter

$$\Gamma_B = -\frac{(\partial S/\partial B)_T}{T (\partial S/\partial T)_B} = -G_r \frac{1}{B - B_c} \quad (14)$$

with the prefactor given by

$$G_r = \frac{(d - y_0 z)\nu}{y_0}. \quad (15)$$

Remarkably, all unknown quantities cancel out and one is left with a numerical prefactor that is a combination of *universal* exponents only.^{44,45}

We would like to note that the general low-temperature form Eq. (14) holds not only at quantum phase transitions, but also for the ideal paramagnet (compare Eq. (9)) as well as certain highly degenerate critical points related to localized magnons^{29,30,31,32,33} where one can apply similar scaling arguments as above.

3. Concepts for magnetic cooling

As described in section 2, the process of magnetic cooling is closely related to the magnetic entropy S_{mag} of the coolant and the way S_{mag} varies with magnetic field and temperature. Generally, the precondition for an effective magnetic cooling is a large absolute value of S_{mag} in the temperature range of interest together with a large $\partial S/\partial B$. The concept of magnetic cooling can be visualized particularly clearly for paramagnets, whose total molar entropy is given by

$$S_{\text{mag}} = R \cdot \ln(2s + 1), \quad (16)$$

with R the gas constant and s the spin value. Due to weak magnetic interactions between the ions, inevitable for any real material, the degeneracy is (at least partly) lifted. As a consequence real paramagnets exhibit, depending on their spin state, a Schottky-like anomaly, $C_{\text{mag}}^{\text{Sch}}$, in their magnetic specific heat. The maximum in $C_{\text{mag}}^{\text{Sch}}$ is located at a temperature T_{max} which corresponds to about half of the zero-field splitting $T_{\text{max}} \sim 0.5 \Delta/k_B$. Due to the Zeeman-effect, the level splitting further increases with increasing field and the Schottky-like anomaly is shifted to higher temperatures. In other words, the corresponding variation of S_{mag} with T and B for a paramagnetic material is determined by the zero-field splitting of the magnetic energy levels and can easily be varied with an external magnetic field. This is illustrated in Fig. 1 with the specific heat of an ideal paramagnet and a more realistic spin-5/2 model paramagnet (with a small single-ion anisotropy) in an external magnetic field of $B = 10$ mT. On the one hand, the isentropes for the ideal paramagnet would go to $T = 0$ as $B \rightarrow 0$ while the lowest accessible temperature in a real paramagnet is determined by the zero-field gap. On the other hand, we infer from Fig. 1 that the ability of an ideal paramagnet in a magnetic field of 10 mT to exchange heat with a cooling load would be limited to a narrow temperature window around 10 mK, while that of a more realistic paramagnet extends to higher temperatures.

Figure 2 (left panel) shows an adiabatic demagnetization process for a model paramagnet (black and grey solid lines) with spin $s = 1/2$ and a zero-field splitting of 0.1 K. The process starts with an isothermal magnetization (from A to B) at an initial temperature $T_i = 1.2$ K, a typical value for a precooling stage to which the heat of magnetization is released. This process is followed by an adiabatic demagnetization (from B to C). The black solid line is the magnetic entropy at zero field $S_{\text{mag}}(T, B = 0)$, whereas the grey solid line corresponds to the magnetic entropy at a finite field, here $B = 2.8$ T. With $T_i = 1.2$ K and a starting field $B_i = 2.8$ T a final temperature $T_f = 0.062$ K is reached at a final field $B_f = 0$ T. The linear variation of temperature with field, shown by the solid black line in the right panel of Fig. 2, corresponds to a constant cooling rate dT/dB over the whole range of operation (see also inset of Fig. 2). Whereas the cooling rate dT/dB of a paramagnet does not depend on the spin state s , the amount of heat the system is able to absorb during the cooling process does depend on s , see section 4. The typical range of operation for paramagnets includes magnetic fields varied between a few Tesla and zero. In

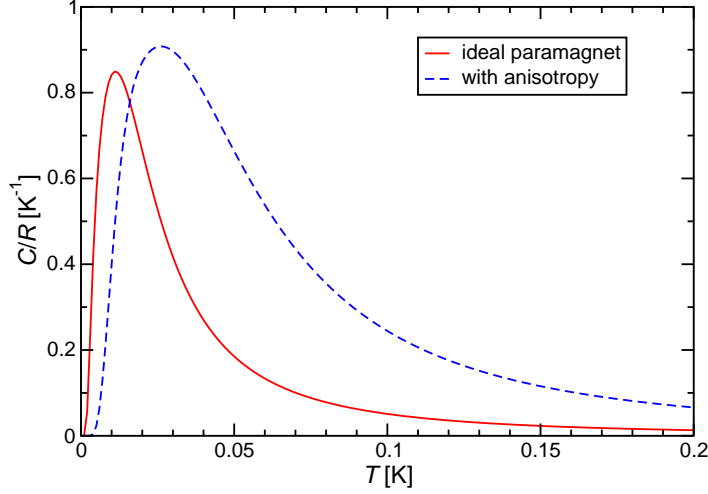


Fig. 1. Specific heat of an ideal and a realistic spin-5/2 paramagnet in a magnetic field $B = 10$ mT. For the ideal paramagnet, the energy function is $E(S^z) = -g \mu_B B S^z$; for the other case we use a model for the ferric ammonium alum with $E(S^z) = D_2 (S^z)^2 + D_4 (S^z)^4 - g \mu_B B S^z$ and $D_2/k_B = -85$ mK, $D_4/k_B = 12$ mK⁴⁶. The spectroscopic g factor is 2 in both cases.

their pioneering work Giauque and MacDougall studied the low-temperature magnetocaloric properties of paramagnetic $\text{Gd}_2(\text{SO}_4)_3 \cdot 8\text{H}_2\text{O}$ and demonstrated that a temperature of 0.53 K could be reached by adiabatic demagnetization.² Nowadays paramagnets are mainly used for cooling to sub-Kelvin temperatures ($0.02 \text{ K} \leq T \leq 1.2 \text{ K}$), with a range of operation for a given salt typically stretching over about one and a half decade in temperature. These systems represent a suitable alternative to ^3He - ^4He dilution refrigerators – the present standard technology for continuous operation at $T < 1 \text{ K}$ – when low costs or ease of operation is in demand. However, they are of great importance for application at microgravity where standard dilution refrigerators are not operational. For the status of gravity-insensitive dilution refrigerators, see Ref.⁴⁷ and references cited therein. Since for space applications, cooling efficiency is of crucial importance, those state-of-the-art paramagnetic coolants used there may serve as good reference materials when discussing performance characteristics of any new material, see section 4.

3.1. Quantum-critical systems

The research on materials in the vicinity of a QCP has been of high current interest, as quantum criticality, reflecting critical behaviour arising from quantum instead of thermal fluctuations, may hold the clue for understanding various intriguing material properties.^{48,49} Generally, a QCP can be reached upon tuning an external parameter r such as pressure, chemical composition or magnetic field to a critical value. Although the critical point at $T = 0$ is inaccessible by experiment, its presence can affect the material's properties significantly over a wide range of temperatures.

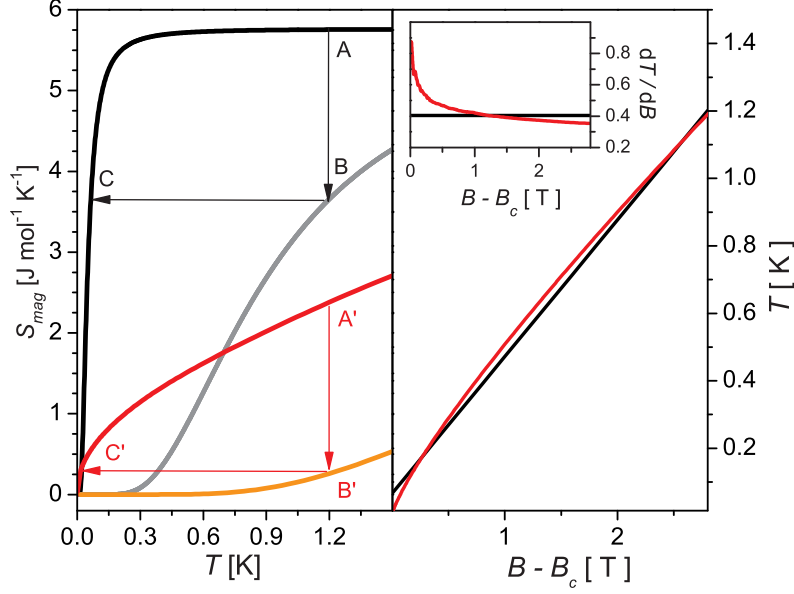


Fig. 2. Left panel: Calculated magnetic entropy S_{mag} of a spin $s = 1/2$ model paramagnet (PM) with a zero-field gap of 100 mK at $B = 0$ T (black solid line) and at 2.8 T (grey line). Also shown is the magnetic entropy as a function of temperature for an ideal $s = 1/2$ antiferromagnetic Heisenberg chain (AFHC), which is inherently quantum critical, with an intra-chain coupling constant of $J/k_B = 3.2$ K at two different field values. The red solid line corresponds to the saturation field of $B_s = 4.1$ T, which marks the endpoint of a quantum-critical line in the material's $B - T$ phase diagram. The orange line shows the entropy at $B = 7$ T where the system is in the field-induced fully polarized ferromagnetic state. Right panel: cooling curves of the PM (black solid line) and the AFHC (red solid line) for a field reduction of $\Delta B = -2.8$ T and a starting temperature of 1.2 K. Note that for the PM the sweep starts at $B_i = 2.8$ T and terminates at $B_f = 0$ whereas for the AFHC it starts at $B_i = 6.9$ T and terminates at $B_f = B_c = 4.09$ T. Inset: Cooling rate dT/dB of the PM (black solid line) and the AFHC (red solid line).

^{48,49} The thermodynamic properties of a material in the vicinity of a QCP are expected to show anomalous power laws as a function of temperature and, even more spectacular, to exhibit an extraordinarily high sensitiveness on these tuning parameters.^{44,45} As we have reviewed in section 2, a diverging magnetic Grüneisen parameter Γ_B is expected for a B -induced QCP,^{44,45,30} and has indeed been recently observed.^{50,51,52} As has been first suggested by J. C. Bonner *et al.*⁵³ and demonstrated by B. Wolf *et al.*,⁵² this critically enhanced Grüneisen parameter around the QCP can be used in principle for an efficient magnetic cooling.

3.1.1. Antiferromagnetic spin-1/2 Heisenberg chain

The uniform spin $s = \frac{1}{2}$ antiferromagnetic Heisenberg chain (AFHC), where only nearest-neighbour spins at site i and $i + 1$ interact via the Heisenberg exchange

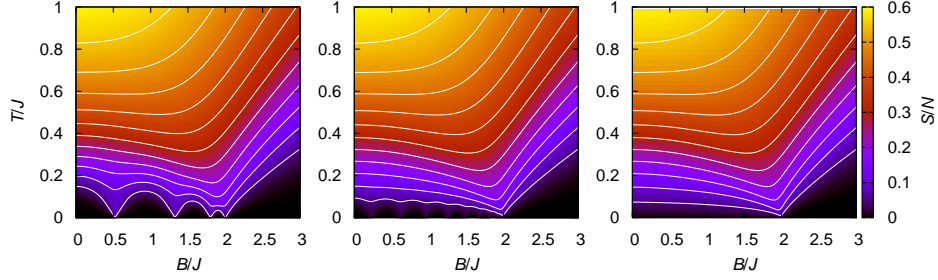


Fig. 3. Entropy per spin S/N of the uniform spin-1/2 antiferromagnetic Heisenberg chain as a function of magnetic field B and temperature T . The left panel shows the result for a ring with $N = 8$ spins, the middle panel for $N = 20$, and the right panel for the thermodynamic limit $N = \infty$. White contour lines start at the bottom with an entropy $S/N = 0.05$ per spin and increase in steps of 0.05. In this figure we use units such that $g\mu_B = 1$. The saturation field $B_s = 2J$ marks a quantum critical point; for $B < B_s$ the system is in a gapless Luttinger-Liquid phase whereas for $B > B_s$ it is gapped.

interaction J along one crystallographic direction, represents one of the simplest quantum-critical system. It is described by the Hamiltonian

$$H = J \sum_{i=1}^N \vec{S}_i \cdot \vec{S}_{i+1} - g\mu_B B \sum_{i=1}^N S_i^z. \quad (17)$$

Here $J > 0$ is the exchange constant, S_i are spin-1/2 operators at site i , g is spectroscopic splitting factor and μ_B the Bohr magneton. This model, despite its simplicity, contains a wealth of non-trivial physics. The peculiar feature of the AFHC is that its quantum-critical behaviour, which is that of a Luttinger liquid (LL), governs the material's properties over wide ranges in temperature and energy (see, e.g., Ref. ⁵⁴ for a summary). The AFHC remains in the LL quantum-critical state for fields up to the saturation field $g\mu_B B_s = 2J$. ⁵⁵ Since the fully polarized state above B_s is a new eigenstate of the system, different from that of the LL quantum-critical state, B_s marks the endpoint of a quantum-critical line in the $B - T$ plane. This is illustrated in Fig. 3 whose left panel shows “historic” ^{56,57} results with $N = 8$, the middle panel $N = 20$, ³⁰ and the right panel the exact solution for the thermodynamic limit $N = \infty$. ⁵⁴ First, we observe that finite-size effects are only relevant in the LL regime $B < B_s$ and at low temperatures. Historically, an important question was if the entropy goes to zero in the limit $T \rightarrow 0$, and it was concluded already on the basis of the results for $N = 8$ that this is indeed the case. ⁵⁶

The white lines in Fig. 3 show constant entropy curves (isentropes) and thus temperature as a function of field during an adiabatic (de)magnetization process. Indeed, it was recognized early on by Bonner *et al.* ^{53,58} that the AFHC exhibits an enhanced MCE and is therefore of interest for being used for magnetic cooling. In the vicinity of the QCP at $B = B_s$ magnetic entropy is accumulated as a consequence of the competition between the different ground states on both sides. This leads to

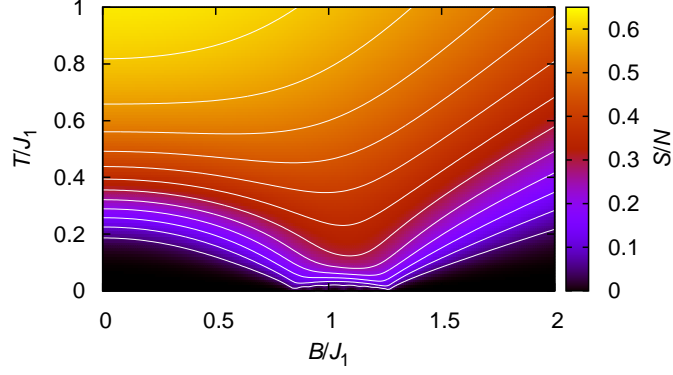


Fig. 4. Entropy per spin S/N of a dimerized spin-1/2 Heisenberg chain with $J_2 = 0.27 J_1$ and $N = 20$ spins. White contour lines start at the bottom with an entropy $S/N = 0.05$ per spin and increase in steps of 0.05. In this figure we use units such that $g\mu_B = 1$. In this case, there are two quantum critical points: one at the saturation field $B_s = 1.27 J_1$ and one at $B_c \approx 0.838 J_1$. For $B_c < B < B_s$ the system is in a gapless Luttinger-Liquid phase whereas for $B < B_c$ or $B > B_s$ it is gapped.

a minimum of the isentropes above this QCP, i.e., a cooling effect upon approaching this QCP. In order to give a first impression on some of the cooling characteristics of such a quantum-critical system, we show in Fig. 2 the relevant quantities of an AFHC in comparison with those of a paramagnet. The cooling performance of a good realization of an AFHC will be discussed in detail in subsection 3.3.3. As Fig. 2 illustrates, quantum-critical systems are of particular interest when an efficient cooling to (in principle) arbitrarily low temperatures is in demand.

3.1.2. Dimerized spin-1/2 Heisenberg chain

Let us briefly review a second prototypical system, namely a “dimerized” $s = 1/2$ Heisenberg chain where two different exchange constants J_1 and J_2 alternate. Historically, MCE measurements on copper nitrate ($\text{Cu}(\text{NO}_3)_2 \cdot 2.5\text{H}_2\text{O}$)^{59,60} prompted theoretical investigations of the MCE in the corresponding spin-1/2 dimer chain model^{61,62,63}. Figure 4 shows the entropy as a function of field and temperature for the historical parameters $J_2 = 0.27 J_1$.⁶³ Although this is a chain with 20 spins (10 dimers), the strong dimerization $J_2/J_1 = 0.27$ ensures that finite-size effects are negligible except for $g\mu_B B$ comparable to J and very low temperatures. In this case, there are two QCPs: one at the saturation field $g\mu_B B_s = J_1 + J_2 = 1.27 J_1$ and another one at $g\mu_B B_c \approx 0.838 J_1$. The system is gapped for $B < B_c$ or for $B > B_s$ and in a gapless LL state for $B_c < B < B_s$. Accordingly, one finds a strong cooling effect for adiabatic field variations $B \nearrow B_c$ or $B \searrow B_s$ and comparably small temperature variations in the LL state.

Recently, the exchange couplings of copper nitrate have been refined using inelastic neutron scattering⁶⁴ and there are new experimental results for the MCE available (see, e.g., Ref. ⁶⁵). One challenge that remains is to provide a quantita-

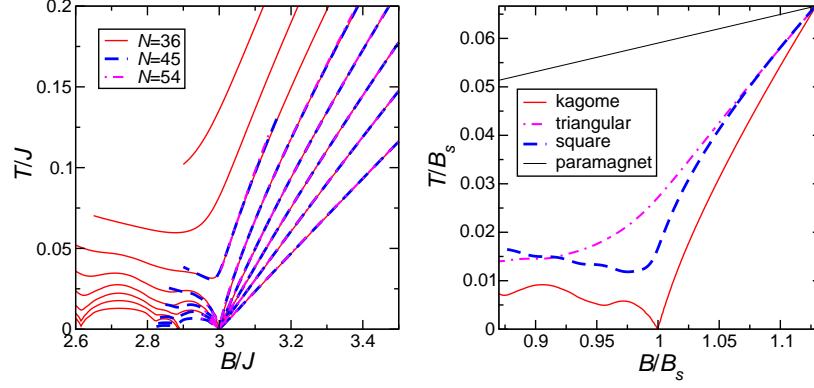


Fig. 5. Left panel: Isentropes for the spin-1/2 Heisenberg model on the kagome lattice close to the saturation field $B_s = 3J$. Lines start at the bottom with an entropy $S/N = 0.025$ per spin and increase in steps of 0.025. Right panel: Comparison of an adiabatic demagnetization process of a spin-1/2 Heisenberg model on the kagome, triangular, and square lattice. The system size is $N = 36$ in all three cases. Also included is the straight line characteristic of an ideal paramagnet. In both panels we use units such that $g\mu_B = 1$.

tive description close to the ordering transition of copper nitrate at $T \lesssim 150$ mK⁶⁵ which is beyond the simple dimerized chain model.⁶³ The ordering transition is captured qualitatively by a dimer mean-field theory,^{61,62} but this theory is not appropriate for describing the LL state. A chain mean-field theory might provide a reasonable alternative for describing the MCE of the coupled-chain system, as has been demonstrated for similar situations.⁶⁶

3.1.3. A highly frustrated magnet: spin-1/2 Heisenberg model on the kagome lattice

Lastly we illustrate the effect of geometric frustration using the spin-1/2 Heisenberg model on a prototypical frustrated lattice: the kagome lattice. The left panel of Fig. 5 shows exact diagonalization results for different system sizes close to the saturation field $g\mu_B B_s = 3J$. Although some extremely big matrices have been diagonalized in this context, systems with $N \geq 36$ spins are too big to allow for a full diagonalization. Therefore, we have performed a low-energy approximation using low-energy states. This in turn implies that one has to restrict the field range of some isentropes in order to render truncation effects small, compare also Refs. 15,67. Comparison of the different system sizes shown in the left panel of Fig. 5 shows that finite-size effects are small, at least for $B \gtrsim B_s$. This reveals a remarkable property: the third law of thermodynamics is violated in this model – there is a finite zero-temperature entropy at the saturation field $B = B_s$. Accordingly, any adiabatic process starting with an entropy less than this zero-temperature entropy necessarily goes to $T = 0$ as $B \rightarrow B_s$. With the help of the localized magnon ground-states one can give lower bounds for the zero-temperature entropy^{29,30,33} and show rigorously

that it is indeed finite. Inspection of the ground-state degeneracies³³ corresponding to the data in the left panel of Fig. 5 yields the estimate $S/N \approx 0.13$ for the zero-temperature entropy, amounting to about 18% of the total entropy of the system. However, for $B < B_s$, the ground-state degeneracy of the classical system is lifted by quantum fluctuations and one obtains a certain amount of heating if one decreases the magnetic field further below B_s .

In order to illustrate the importance of geometric frustration, we imagine the following thought experiment: we take the non-frustrated square lattice as well as the frustrated triangular lattice and normalize the energy scale such that the quantum critical points at $B = B_s$ coincide. Then we start at one point in the (B, T) -plane and compare the adiabatic demagnetization processes of the different systems. This is implemented in the right panel of Fig. 5 which shows one isentrope each for the spin-1/2 Heisenberg model on the square, triangular,⁶⁷ and kagome lattice, using systems with $N = 36$ spins in all three cases. We also include the straight line characteristic for an ideal paramagnet. Evidently, any quantum critical system outperforms the ideal paramagnet in this field range and the highly frustrated kagome lattice outperforms the other systems in the sense that one can theoretically reach arbitrarily low temperatures. The right panel of Fig. 5 suggests that the non-frustrated square lattice outperforms the frustrated triangular lattice in the sense that a lower temperature is reached close to the saturation field for these particular initial conditions. Nevertheless, other aspects also need to be kept in mind. In particular, the entropy per spin along these isentropes is $S/N = 0.0258$, 0.067 , and 0.1 for the square, triangular, and kagome lattice, respectively. Thus, with increasing frustration, the amount of entropy increases that is available for the exchange of heat with a cooling load.

In any real system, the third law of thermodynamics will of course be restored, thus limiting the smallest temperature that one can reach. Still, one may hope some of the good properties of a highly frustrated magnet to be preserved in a relevant temperature range.

3.2. Interacting ultracold gases

Large theoretical and experimental efforts have been devoted to revealing the mechanisms behind magnetic ordering and superconductivity of quantum many-body systems. Due to the high level of complexity in solid state systems, a quantitative comparison between microscopic theory and experiment can be a challenging task. It is therefore highly desirable to work with systems that are able to simulate the original solid state many-body systems, but with a higher degree of tunability and control.

Over the past decade, ultracold quantum gases in optical lattices have provided an excellent laboratory for investigating quantum many-body physics.^{68,37} Optical lattices of different geometry (triangular, hexagonal, kagome) have been created,^{69,70} and Mott insulating phases (bosonic, fermionic) realized,^{38,39} to mention just

a few of the relevant developments. Correlated atom tunneling and superexchange couplings have been observed,⁴¹ as well as short-range magnetic correlations.⁴⁰ New single-atom in-situ detection techniques with single-site resolution, based on the quantum-gas microscope,⁷¹ allow the detection of magnetic excitations and their dynamics.⁷² A quantum simulation of the Ising model in a transverse magnetic field and its ordering transition have been achieved via mapping to a tilted Mott insulator and single-site resolved detection.⁴² One major current goal of the field is to simulate the phase diagram of the fermionic Hubbard model, including antiferromagnetic long-range magnetic order.³⁶ More generally, it has been shown that also bosonic two-component gases allow for tunable (ferro- and antiferromagnetic) spin order.^{73,74,75} The corresponding critical temperatures are defined by the superexchange scale and have not been reached yet in experiments.⁴³ While *average* entropies per particle down to $S/k_B N = 0.5$ have been demonstrated for fermions in pure dipole traps, in optical lattices only values down to $S/k_B N = O(1)$ could be realized so far.⁷⁶ Note that in most cases the entropy density in the center of the optical trap is significantly lower. Nevertheless, it is so far above the critical entropy per particle for long-range magnetic order in a lattice, which for the fermionic case (Néel order) has been calculated as $S_c/N \approx 0.5k_B \ln 2 = 0.35k_B$,⁷⁷ while for two-component bosons in $d = 3$ it has been shown that the critical entropy depends on the type of long-range order: it is given by the value $S_c/N \approx 0.5k_B$ for the z-Néel state (where only a discrete Ising-symmetry is broken) and the lower value $S_c/N \approx 0.35k_B$ for the xy-ferromagnet (where, analogously to spin-1/2 fermions, a continuous symmetry is broken, in this case $U(1)$).⁷⁸

In order to reach these low entropies, which are characteristic for strongly correlated states with magnetic order, new cooling techniques in the presence of the optical lattice need to be implemented. Note that direct evaporative cooling – the standard approach to degenerate quantum gases – is in general not efficient in the lattice due to low scattering rates.⁷⁶ A further challenge in this context is the *dynamical arrest* of many-body dynamics, which was recently discovered for a strongly interacting fermionic mixture. It leads to departure from adiabatic evolution of the atomic cloud when the lattice is ramped up,⁷⁹ and therefore implies a higher entropy in the final state. To avoid this effect, cooling schemes which avoid global mass- or entropy transport could be preferable.⁸⁰

Inspired by solid state systems, adiabatic demagnetization cooling of an ultracold gas has been performed,⁸¹ with final temperatures in the μK range. However, so far this technique has only been applied for ^{52}Cr , which has a high magnetic moment and therefore a high dipolar relaxation rate.⁸¹ This approach has not yet been implemented in combination with an optical lattice.

On the other hand, a related technique – spin-gradient thermometry and cooling – has been realized for a mixture of two hyperfine states of ^{87}Rb in a 3D optical lattice,^{82,83} and theoretically simulated.⁸⁴ Here, the ultracold Bose gas is prepared in a magnetic field gradient, which separates the two spin components to opposite sides of the trap. The width of the transition layer between two hyperfine

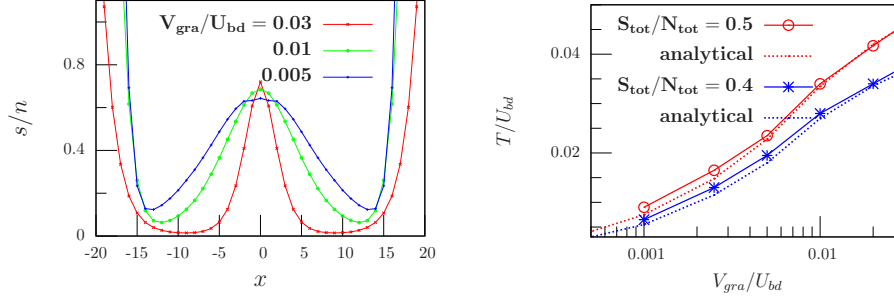


Fig. 6. Spin-gradient demagnetization cooling. Left: Field-gradient dependence of the distribution of the local entropy per particle along the x direction on the $y, z = 0$ axis, for an average entropy per particle $S_{tot}/N_{tot} = 0.7$. The red, green and blue lines correspond to field gradient values of $V_{gra}/U_{bd} = 0.03, 0.01$ and 0.005 . Right: Adiabatic spin-gradient demagnetization cooling in a cubic lattice. Results are obtained by BDMFT+LDA and compared to an analytical zero-tunneling approximation in the atomic limit.⁹⁰ Interaction parameters are set to $U_b = U_d = 1.01U_{bd}$, and the hopping amplitudes are given by $2zt_b = 2zt_d = 0.12U_{bd}$, with a total particle number $N_{tot} \approx 17000$ in a harmonic trap $V_0 = 0.0025U_{bd}$. Figures taken from ⁸⁴.

spin domains serves as an accurate thermometer for temperatures in the nK regime, and entropies in a broad range $0.1 < S/Nk_B < \ln 2$. As the gradient is lowered, the two spin components mix, and entropy from particle-hole excitations is transferred into the spin mixing entropy. Using bosonic dynamical mean-field theory (DMFT), we have quantitatively verified that this leads to a cooling effect for the interacting many-body system, and shown that the magnetically ordered regime (XY ferromagnet) can be reached in this way,^{84,85} see Fig. 6. In the following we give more details. The Hamiltonian of the two-component bosonic ⁸⁷Rb system is given by

$$\begin{aligned} \mathcal{H} = & - \sum_{\substack{\langle i,j \rangle \\ \nu=b,d}} t_\nu (b_{i\nu}^\dagger b_{j\nu} + h.c.) + \frac{1}{2} \sum_{i,\lambda\nu} U_{\lambda\nu} \hat{n}_{i\lambda} (\hat{n}_{i\nu} - \delta_{\lambda\nu}) \\ & + \sum_{i,\nu=b,d} (V_i - \mu_\nu) \hat{n}_{i\nu} - \sum_{i,\nu} \mu_{mag}^\nu B(x_i) \hat{n}_{i\nu} \end{aligned} \quad (18)$$

where we include a linear position-dependence of the magnetic field in x direction, $B(x_i) = cx_i$ where c is the magnetic field gradient and x_i the distance from the harmonic trap center, as in the experiment.⁸³

Here $\langle i, j \rangle$ denotes the summation over nearest neighbours sites and the two bosonic species (hyperfine states) are labeled by the index $\lambda(\nu) = b, d$. These two species can in general have different hopping amplitudes t_b and t_d , due to a spin-dependent optical lattice. We denote the bosonic creation (annihilation) operator for species ν at site i by $b_{i\nu}^\dagger$ ($b_{i\nu}$) and the local density by $\hat{n}_{i,\nu} = b_{i\nu}^\dagger b_{i\nu}$. $U_{\lambda\nu}$ are the inter- and intra-species interactions, which are tunable via Feshbach resonances or by a spin-dependent lattice. For ⁸⁷Rb we assume the couplings $U_{bb} \approx U_{dd} \approx U_{bd}$ to be approximately equal, which was the case in the experiment.⁸³ μ_ν denotes the global chemical potential for the two bosonic species, while V_i is the harmonic potential

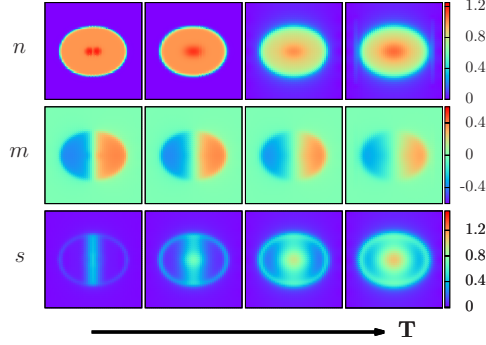


Fig. 7. Real-space distribution (in the $z = 0$ plane of a 3D cubic optical lattice) of the local particle density n , magnetization m and entropy s , calculated by BDMFT+LDA. From left to right, the temperature is increasing as $T/U_{bd} = 0.020, 0.040, 0.070$ and 0.095 , respectively. The interactions are $U_b = U_d = 1.01U_{bd}$ and the hopping amplitudes are set to $2zt_b = 2zt_d = 0.12U_{bd}$, with a total particle number $N_{tot} \approx 17000$ in a harmonic trap of strength $V_0 = 0.004U_{bd}$ and a magnetic field gradient $V_{gra} = 0.01U_{bd}$. Figure taken from ⁸⁴.

due to the optical trap, and μ_{mag}^ν is the magnetic moment of component ν . Bosonic dynamical mean-field theory (BDMFT) ^{86,75,87,88,89} provides a non-perturbative description of strongly correlated bosons on a lattice at zero- and finite-temperature. We have recently developed a *real-space* version of BDMFT (RBDMFT), ⁸⁵ in order to take into account inhomogeneities such as an external trapping potential or disorder. The results presented here have, however, been obtained by a local density approximation (LDA) scheme in combination with single-site BDMFT. The advantage of this approach lies in the larger system size accessible. In these calculations, the local chemical potential is adjusted according to the trapping potential, i.e., $\mu_\nu(r) = \mu_\nu - V_0 r^2$, where V_0 characterizes the strength of the harmonic confinement and r is the distance from the center of the trap. We have benchmarked the validity of the LDA+BDMFT approach by a quantitative comparison with the more rigorous RBDMFT method.

A direct calculation of the entropy within BDMFT is problematic. But, assuming that the system is in thermodynamic equilibrium, we can apply a Maxwell relation to obtain the local entropy per site at temperature T and chemical potential $\mu_s(r) = (\mu_b(r) + \mu_d(r))/2$:

$$s(\mu_s(r_0), T) = \int_{-\infty}^{\mu_s(r_0)} \frac{\partial n(r)}{\partial T} d\mu_s(r) \quad (19)$$

where $n(r) = n_b + n_d$ denotes the local density (*i.e.*, number of particles per lattice site) at a distance r from the trap center. Note that the thermodynamic relation (19) is only valid at fixed difference of the chemical potentials $\Delta\mu(r) = \mu_b(r) - \mu_d(r)$ for the two-component mixture. (R-)BDMFT yields density distributions which are

accurate enough to allow for a precise evaluation of the derivative $\frac{\partial n}{\partial T}$. The relation (19) has been used to obtain the entropy distributions which will be discussed in the following.

The spin-gradient cooling scheme is based on the inhomogeneous entropy distribution of the trapped system, as shown in Fig. 7. During the demagnetization process, the local entropy per particle in the spin-mixed regions decreases. For the fillings considered here, three different spatial regions correspond to different phases of the system: the superfluid, the spin-mixed and the single-component Mott-insulating regions. For large initial values of the field gradient, the superfluid and the spin-mixed region carry most of the entropy of the system, while the entropy in the single-component Mott insulator regions is negligible. With decreasing magnetic field gradient, the spin-mixed region expands, while the single-component Mott-insulating region shrinks. At the same time, the temperature drops, although entropy carried by hot mobile particles is drained into the expanding mixed region, since the local entropy *per particle* in the central spin-mixed region decreases. In the left panel of Fig. 6, we show the local entropy per particle s/n at different field gradient strengths for fixed total particle number and entropy. It is clearly visible that s/n decreases in the central region as the field gradient is adiabatically reduced. As a result, the temperature decreases from $T/U_{bd} = 0.065$ to 0.035 when the field gradient is reduced from $V_{gra}/U_{bd} = 0.03$ to 0.005 . The resulting spin gradient demagnetization cooling efficiency is displayed in the right panel of Fig. 6. Our result from BDMFT simulations is in good agreement with analytic results from the zero-tunneling (atomic) limit,⁹⁰ since in our description of the experiment we choose a deep optical lattice which leads to a small hopping t_ν/U_{bd} . The adiabatic demagnetization cooling appears to be less efficient at larger values of the field gradient, since in this case the trap center becomes superfluid, with enhanced entropy capacity.

Spin-gradient cooling efficiency may be additionally limited by magnetic correlations when the temperature is of the order of the super-exchange energy,⁸³ and (dynamically) by the fact that it requires global entropy transport. The latter problem is avoided by proposals based, e.g., on superlattices,⁸⁰ which require only local mass and entropy transport on length scales of the order of the lattice constant, and may thus allow creating Néel-ordered states, starting from a low-entropy band insulator.

A further many-body phenomenon leading to interaction-enhanced cooling is the *Pomeranchuk effect*, which was first discovered in ^3He , where heating leads to increased localization due to the higher (nuclear) spin entropy of the solid phase. An analogous phenomenon occurs within the Hubbard model, where at intermediate coupling strengths the spin entropy of the Mott insulator $S/N \approx k_B \ln 2$ is higher than that of the Fermi liquid.⁷⁷ Recently a similar effect was discovered for spinful bosonic mixtures, e.g., of two hyperfine states of ^{87}Rb , where upon heating of the strongly correlated, non-ordered superfluid phase (Fig. 8, dotted line) the system en-

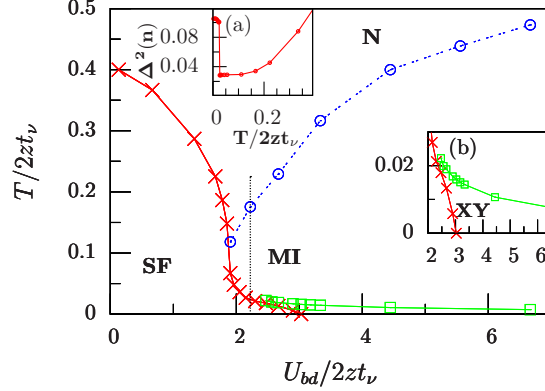


Fig. 8. Pomeranchuk effect in spinful ultracold bosons. Upon heating of the strongly correlated, non-ordered superfluid (SF) phase along the dotted line shown the system enters into the paramagnetic Mott insulator (MI), which has the higher spin entropy $S/N \approx k_B \ln 2$. This results in a drastic reduction and non-monotonic temperature-dependence of local number fluctuations $\Delta(n_i)$, which could be measured in-situ with the optical quantum-gase microscope,⁷¹ and occurs at higher temperatures/entropies than the transition into the long-range ordered phase with xy-ferromagnetism (below the green line). Figure taken from⁸⁴.

ters into the paramagnetic Mott insulator, which again has the higher spin entropy $S/N \approx k_B \ln 2$.⁸⁴ This results in a drastic reduction and non-monotonic temperature dependence of the local particle number fluctuations $\Delta^2(n_i) = \langle \hat{n}_i^2 \rangle - \langle \hat{n}_i \rangle^2$ on a single site, which could be measured in-situ with the optical quantum-gas microscope.⁷¹ Since this effect occurs at temperatures and entropies above the magnetic ordering scale, it may be more easily accessible experimentally than long-range magnetic order. The Pomeranchuk effect also leads to enhanced adiabatic cooling beyond noninteracting band structure effects.^{36,77} In Fig. 9 we show results for the spin-1/2 Fermi-Hubbard model, including mass (hopping) imbalance.^{91,92} Preparing a low-entropy degenerate mixture, followed by adiabatic loading into a shallow lattice and ramp-up of the lattice, leads to a Néel-ordered state (grey region). Note that the critical entropy is overestimated by DMFT as $S_c/N \approx k_B \ln 2$, as is the magnitude of the Pomeranchuk effect, which for fermions has been shown to decrease due to short-range magnetic correlations not captured by DMFT.⁹³ The DMFT estimate for S_c becomes, however, more accurate for the hopping-imbalanced system, where the full $SU(2)$ symmetry is broken down to $Z_2 \times U(1)$, which leads to a gapped excitation spectrum and therefore constitutes a promising route towards superexchange-mediated quantum magnetism. The Pomeranchuk effect has been demonstrated experimentally for ultracold fermionic ^{173}Yb mixtures with internal symmetry $SU(N)$ up to $N = 6$, where it has been shown that the corresponding larger value of the (hyperfine) spin enhances the magnitude of the adiabatic cooling effect and leads to lower temperatures in the final Mott-insulating state.⁹⁴ In a related work on high-spin fermions, it has been pointed out that inhomogeneous

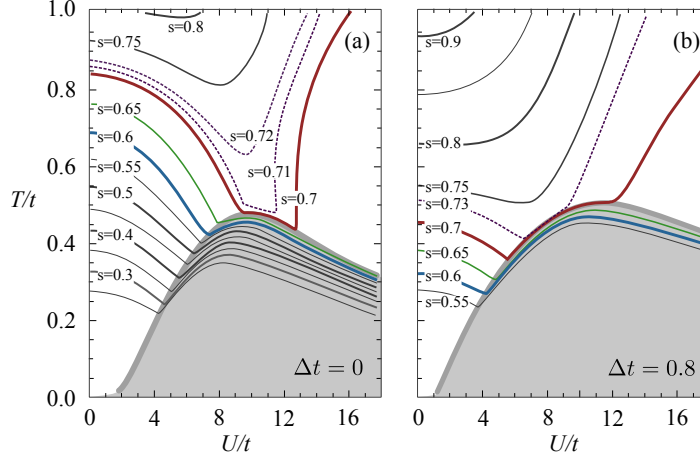


Fig. 9. Pomeranchuk cooling of ultracold fermions with spin-1/2. Preparing a low-entropy degenerate mixture, adiabatic loading into a shallow lattice and ramp-up of the lattice creates a Néel-ordered state (grey region). Note that the critical entropy is overestimated by DMFT as $S/N \approx k_B \ln 2$. This DMFT estimate becomes more accurate for the hopping-imbalanced system b). Figure taken from ⁹¹.

entropy profiles in the presence of an optical trap and a spatially variable quadratic Zeeman coupling may lead to highly efficient adiabatic cooling of an effective spin-1/2 core, thus leading to antiferromagnetic order. ⁹⁵

3.3. Magnetic cooling of solid state systems

3.3.1. State-of-the-art paramagnets

Similar to the classical coolant $\text{Gd}_2(\text{SO}_4)_3 \cdot 8\text{H}_2\text{O}$, dilute systems of magnetic ions are used for technical applications. The standard materials are the spin-5/2 containing ferric ammonium alum $\text{Fe}(\text{NH}_4)(\text{SO}_4)_2 \cdot 12\text{H}_2\text{O}$ (FAA), ⁹⁶ the spin-3/2 carrying chromic potassium alum $\text{CrK}(\text{SO}_4)_2 \cdot 12\text{H}_2\text{O}$ (CPA), ⁹⁷ and the effective spin-1/2 compound cerium magnesium nitrate (CMN). ⁹⁸ These materials have in common that they all contain a significant amount of water to dilute the magnetic system. Despite the large distance between the magnetic ions, precluding their direct magnetic exchange interaction, there are still weak residual magnetic interactions which eventually leads to long-range magnetic order in all of these compounds at a critical temperature $T_c \leq 50 \text{ mK}$. The magnetic order leads to a significant reduction of S_{mag} , and therefore T_c marks the lower bound for the accessible temperature range. In addition, on approaching T_c from above, the cooling becomes progressively inefficient. Due to the reduced entropy (as a consequence of incipient short-range ordering), the adiabatic temperature change is smaller than for an ideal paramagnet. In a standard single-stage magnetic cooler the typical field range for the demagnetization process is $0 \leq B \leq 2 \text{ T}$ with an initial temperature $T_i \leq 1.5 \text{ K}$. ⁹⁹ The material CMN, having a T_c of about 2 mK, can be used as a magnetic coolant

down to temperatures even below 5 mK. This has to be compared with the lowest temperature of around 15 mK for CPA and 30 mK for FAA. Since the amount of heat which can be absorbed by a paramagnetic coolant depends on the spin s , FAA ($s = 5/2$) is often used when a large amount of heat has to be removed from the sample. This is the case in some space applications.^{9,10} Due to its entropy distribution as a function of temperature and field, FAA is a practical working substance for a single-stage magnetic cooler. But unfortunately, FAA has a few properties which complicate its use. Among them is the fact that it is corrosive to copper-based alloys. In addition, FAA expands slightly when crystals are formed and undergoes a chemical transition when heated above 40° C which permanently destroys its paramagnetism. Moreover, FAA dehydrates when exposed to vacuum and the resulting powdery substance does no longer act as an effective coolant at low temperatures. This means that special materials together with peculiar techniques are necessary to build the housing of a FAA salt pill.¹⁰⁰ Another problem in connection with all paramagnetic salts is their low thermal conductivity. This problem is usually circumvented by putting some Au-wires inside the salt pill which provide a sufficient thermal contact between the paramagnetic salt and the sample/device to be cooled. An alternative approach for tackling the problem of the low thermal conductivity of paramagnetic salts is the use of paramagnetic intermetallic compounds. They have attracted some attention with respect to their magnetocaloric properties. One of the most studied materials in this context is PrNi₅, which has also been successfully used in nuclear adiabatic demagnetization devices.¹⁰¹

3.3.2. *Frustrated magnets: classical systems*

An enhanced cooling power in comparison to paramagnets can be obtained with magnetic materials exhibiting geometric magnetic frustration because these materials stay in the so-called disordered cooperative paramagnetic state well below the Curie-Weiss temperature.²⁵ Due to their large spin values these materials are labeled as classical systems. A prominent example is Gadolinium gallium garnet Gd₃Ga₅O₁₂ which has long been known as a suitable refrigerant material below 5 K. Effective cooling has been demonstrated down to temperatures of about 0.5 K.²⁴ Another group of geometrically frustrated magnets beside the garnets are Heisenberg antiferromagnets based on the pyrochlore structure.²⁶ They are particularly suited for magnetic cooling as they exhibit the highest degree of frustration and thus the highest cooling rates among all types of geometrically frustrated magnets. The degree of frustration is directly connected to the number of soft magnetic excitations below the saturation field.²⁶ A prototype material of this class is Gd₂Ti₂O₇ where the largest magnetocaloric effect is observed between 12 T and 6 T with a $dT/dB \approx 0.5$ K/T.²⁷ This field range corresponds to a crossover regime between a saturated and the disordered cooperative paramagnetic state.²⁷ It was shown that the cooling rate of Gd₂Ti₂O₇ even exceeds that of Gd₃Ga₅O₁₂ around the satura-

tion field. However, deviations from the ideal classical highly frustrated Heisenberg antiferromagnet limits the lowest accessible temperature T_{\min} during a cooling process. One such correction is given by quantum fluctuations (compare section 3.1.3). Indeed, for $\text{Gd}_2\text{Ti}_2\text{O}_7$ and $\text{Gd}_3\text{Ga}_5\text{O}_{12}$ good agreement with a classical Heisenberg model was observed for $B > B_s$, but deviations were found at low temperatures for $B < B_s$.²⁷ For such reasons, application of these systems is favored for temperatures down to approximately 0.5 K.¹⁰²

3.3.3. Quantum-critical systems

Here we summarize recent results of the MCE on materials close to a quantum critical point. This includes low-dimensional insulating quantum magnets and metallic heavy-fermion materials.

(i) Low-dimensional quantum magnets

There are a number of excellent realizations of quasi-1D quantum magnets such as $\text{Cu}(\text{C}_4\text{H}_4\text{N}_2)(\text{NO}_3)_2$ ¹⁰³ and KCuF_3 ¹⁰⁴ where it has been demonstrated that quantum-critical Luttinger liquid (LL) behavior governs the material's properties over wide ranges in temperature and energy. For quasi-2D antiferromagnets the compounds $[\text{Cu}(\text{pz})_2](\text{ClO}_4)_2$, $[\text{Cu}(\text{pz})_2](\text{BF}_6)_2$ and $[\text{Cu}(\text{pz})_2(\text{NO}_3)](\text{PF}_6)$ are good realizations.¹⁰⁵ However, in most cases the magnetic exchange couplings are too large for a technical application and in the case of KCuF_3 they are of order 100 K, requiring magnetic fields of order 100 T to drive the system quantum critical.

A proof-of-principle experiment, demonstrating an increased cooling rate around B_s , was performed by using a copper-containing coordination polymer $[\text{Cu}(\mu\text{-C}_2\text{O}_4)(4\text{-aminopyridine})_2(\text{H}_2\text{O})]_n$ (labeled CuP in the following)⁵², first synthesized by Castillo *et al.*¹⁰⁶ A comparison of the results of magnetic susceptibility and specific heat measurements on single crystalline material with model calculations¹⁰⁷ showed that CuP is indeed a very good realization of a uniform spin-1/2 AFHC with an intra-chain coupling $J/k_B = (3.2 \pm 0.1)$ K.¹⁰⁸ Compared to other excellent model substances of this kind, such as copper pyrazin dinitrate,¹⁰³ CuP excels by its comparatively small saturation field $B_s = 4.09$ T (for $B \parallel b$)^a. This enables to study the MCE in the relevant field range below about twice the saturation field by using standard laboratory magnets.

In Fig. 10a we show the MCE, approximated by $\Gamma_B = T^{-1}(\Delta T/\Delta B)_{S \approx \text{const}}$, as a function of magnetic field for various constant temperatures. The values of $\Gamma_B(B, T)$ are negative for $B < B_s$, implying that here the material is cooling during the magnetization process, in contrast to the behaviour of a simple paramagnet. Upon increasing the field, $\Gamma_B(B, T)$ passes through a weak minimum for $T < 0.97$ K,

^aFor a new spin-1/2 chain substance with an even smaller saturation field that has also been investigated with regard to magnetocaloric properties, see Ref. ¹⁰⁹.

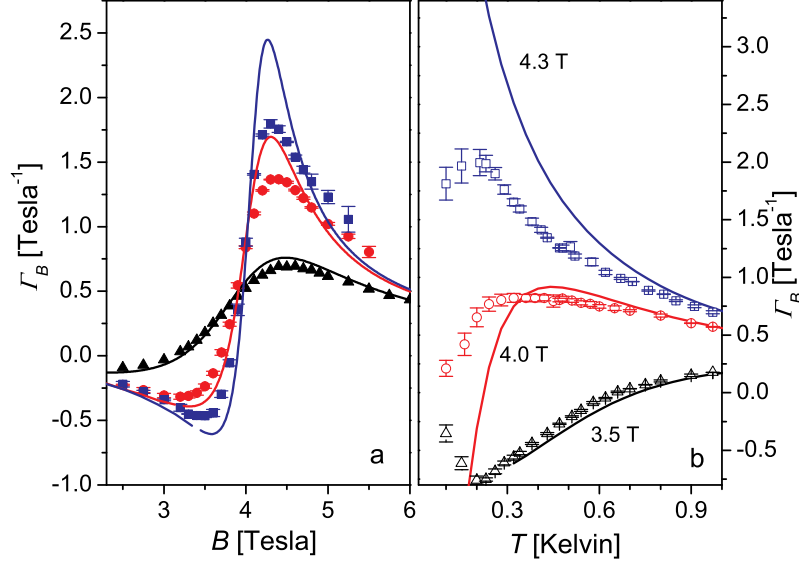


Fig. 10. (a) Experimental data of the magnetic Grüneisen parameter Γ_B (symbols) of single crystalline CuP (a copper-containing coordination polymer – a good realization of a spin-1/2 antiferromagnetic Heisenberg chain) as a function of magnetic field ($B \parallel b$ -axis) at $T = 0.97$ K (black full triangles) $T = 0.42$ K (red full circles) and 0.32 K (blue full squares). The solid lines are the results of quantum Monte Carlo (QMC) simulations and exact diagonalization of a finite-size lattice of the spin-1/2 antiferromagnetic Heisenberg chain for the corresponding temperatures (same colour code) by using $J/k_B = 3.2$ K. A g -value of 2.28 has been used in the calculations to account for a small misalignment of the crystals. (b) The magnetic Grüneisen parameter Γ_B (symbols) of CuP as a function of temperature at constant fields below ($B = 3.5$ T and 4.0 T) and above (4.3 T) B_s . The solid lines (same colour code as used for the experimental data) represent the results of model calculations for the ideal AFHC for the corresponding temperatures. The figure is taken from ⁵².

changes sign, and adopts a pronounced maximum above 4 T. The sign change in $\Gamma_B \propto (\partial S / \partial B)_T$ around B_s implies the presence of a distinct maximum in the magnetic entropy. This is expected around the QCP ⁴⁵ and reflects the accumulation of entropy due to the competition between the neighbouring ground states. The solid line represents calculations of a parameter-free model. The theoretical results are based on exact diagonalization and quantum Monte Carlo simulations, performed by using the experimentally determined exchange-coupling constant $J/k_B = 3.2$ K. ⁵² Figure 10b exhibits the magnetic Grüneisen parameter as a function of temperature at constant field $\Gamma_B(T, B = \text{const})$. The data were taken at fields below ($B = 3.5$ T and 4.0 T) and above ($B = 4.3$ T) the saturation field B_s . While the experimental results nicely agree with the model calculations for the ideal system (solid lines) at higher temperatures $T \geq 0.8$ K, the data progressively deviate from the calculations with lowering the temperature. An anomaly is clearly visible around 0.22 K in Fig. 10b at 3.5 T, 4.0 T, and 4.3 T which is not expected from

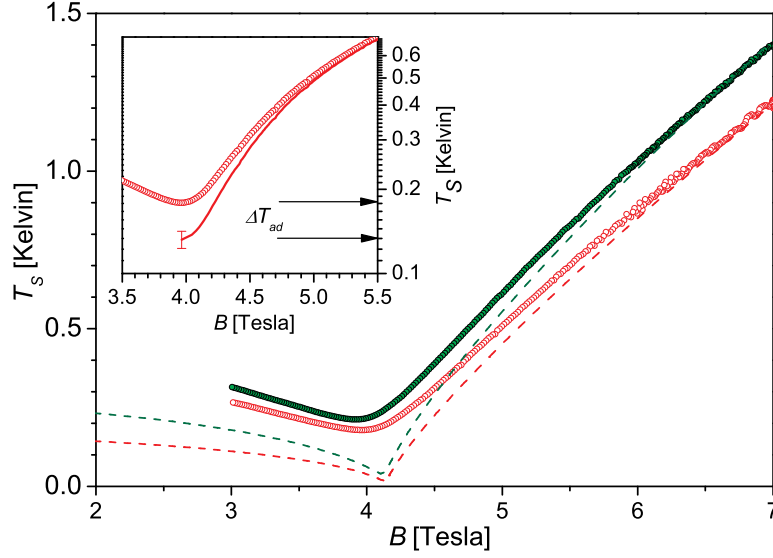


Fig. 11. Sample temperature T_s (symbols) measured upon demagnetizing a collection of CuP single crystals ($B \parallel b$ -axis) of total mass of 25.23 mg under near adiabatic conditions. The initial parameters were set to $B_i = 7$ T and $T_i = 1.40$ K (green symbols) and 1.21 K (red symbols). Broken lines represent ideal isentropes, derived from the exact result for the entropy of the spin-1/2 antiferromagnetic Heisenberg chain⁵⁴ for the same initial parameters as used in the experiment. Inset: Experimental data with $T_i = 1.21$ K (red open symbols) together with data corrected for the parasitic heat load (red solid line).

the theoretical calculations. This feature is likely to be related to the opening of a field-induced gap in the excitation spectrum consistent with the presence of a weak Dzyaloshinskii-Moriya interaction, allowed by symmetry in CuP, which gives rise to a field-induced gap in the excitation spectrum.

Figure 10 demonstrates that the magnetothermal behaviour of CuP deviates from that of an ideal spin-1/2 AFHC especially at low temperatures. This may limit the use of CuP for magnetic cooling.

Therefore in Ref.⁵² demagnetization experiments under improved, near adiabatic conditions were performed to explore the material's potential as a coolant. For these measurements, an array of oriented single crystals of total mass of 25.23 mg was used. Starting from initial parameters B_i and T_i , the field was ramped down at a rate $\Delta B/\Delta t = -0.3$ T/min for $B \geq 6$ T and -0.5 T/min for $B < 6$ T. As Fig. 11 indicates, T_s initially decreases linearly with B such as seen for simple paramagnets where $T/B = \text{const}$. With further decreasing temperature, however, the cooling process becomes superlinear in accordance with the model calculations for the ideal system (broken line in Fig. 11). This enhanced cooling rate is a direct manifestation of quantum criticality. In this test experiment, with a given weak thermal coupling to the surrounding bath (sample holder) which is kept at a temperature of 1.2 K, a minimum temperature of 0.179 K was reached for a starting temperature $T_i =$

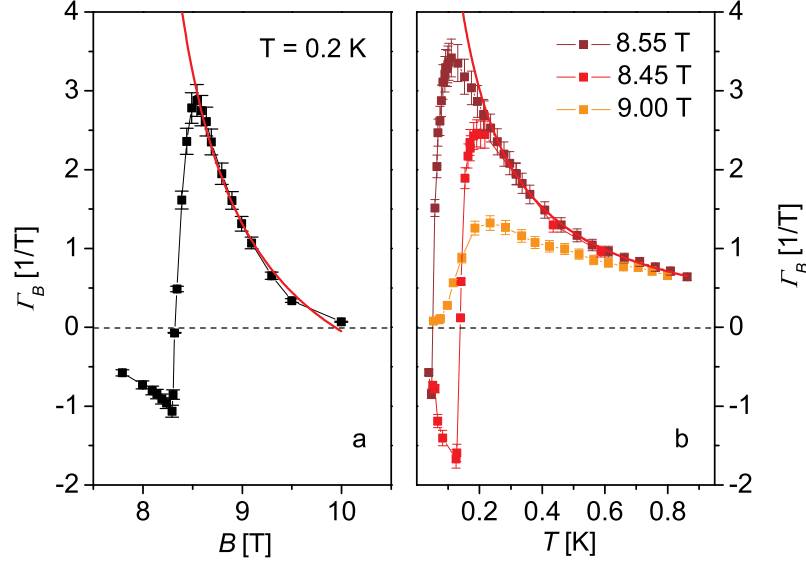


Fig. 12. (a) Data for the magnetic Grüneisen parameter Γ_B of single crystalline Cs_2CuCl_4 for $B \parallel a$ -axis as a function of field at $T = 0.2$ K. (b) Γ_B as a function of T for constant magnetic fields around the QCP. The solid red lines in both panels indicate an $1/T$ dependence. Figure taken from ⁶⁶.

1.21 K. The effect of the finite parasitic heat load due to non-adiabatic conditions, present to some extent in any cooling experiment, has been estimated in Ref. ⁶⁶ based on simultaneous measurements of the thermal coupling of CuP to the bath. According to these calculations a minimum temperature of 0.132 K is expected under hypothetically ideal adiabatic conditions which corresponds to a temperature reduction of $\Delta T_{ad} \sim 50$ mK, see inset to Fig. 11. These experimental findings indicate that the main source for the deviations between the cooling curve of CuP and the theoretical calculations for $T_s(B)$, indicating an accessible minimum temperature below 20 mK, is likely the above-mentioned perturbing interactions, especially the field-induced excitation gap due to the Dzyaloshinskii-Moriya interaction. On the other hand, the good agreement with the theory curve at higher temperatures, where these interactions are irrelevant, shows that for those realizations of a spin-1/2 antiferromagnetic Heisenberg chain where the perturbing interactions are less strongly pronounced, cooling to much lower temperatures should be possible. As promising candidates we therefore suggest to focus on antiferromagnetic spin-1/2 chain compounds with (i) a sufficiently weak intra-chain coupling J , and (ii) magnetic centres related by inversion symmetry so that the Dzyaloshinskii-Moriya interaction is not active.

As another example for a quantum-critical system, we mention triangular-type frustrated quasi-2D Heisenberg antiferromagnets. Such systems are expected to exhibit an even larger cooling capability as compared to the AFHC as a consequence

of the peculiar entropy landscape which is a result of the geometric frustration of the material, compare section 3.1.3. A good realization of such a system is found in the layered triangular-lattice Heisenberg antiferromagnet Cs_2CuCl_4 where the frustration results from a dominant antiferromagnetic exchange coupling constant $J/k_B = 4.3 \text{ K}$ ¹¹⁰ along the in-plane b -axis and a second antiferromagnetic in-plane coupling $J' \sim J/3$ along a diagonal bond in the bc -plane.¹¹¹ Further couplings in this material include a weak inter-plane interaction $J'' \sim J/20$ and a small anisotropic Dzyaloshinskii-Moriya interaction $D \sim J/20$.¹¹² This material has attracted considerable interest due to the 2D character of its magnetic excitations in certain regions of the $B - T$ phase diagram and its quantum-critical properties.^{110,111,112} The system exhibits a field-induced quantum phase transition at a critical field B_s of about 8.5-9 T, depending on the orientation of the magnetic field. Here B_s separates long-range antiferromagnetic order from a fully-polarized ferromagnetic state.

Figures 12a,b exhibit the results of Γ_B on single crystalline Cs_2CuCl_4 as a function of magnetic field (Fig. 12a) at $T = 0.2 \text{ K}$ and temperature (Fig. 12b) at various constant fields around the QCP which is located at around 8.5 T for $B \parallel a$ ¹¹² used in these experiments. The Γ_B values taken at 0.2 K reveal a sign change at 8.32 T, reflecting the B -induced transition, in accordance with literature results on the $B - T$ phase diagram.¹¹³ For $B < B_s$ $|\Gamma_B|$ is relatively small, indicating a flat entropy landscape in the material's antiferromagnetically ordered state. However, upon increasing the field to above B_s , Γ_B changes sign and adopts a pronounced maximum at about 8.53 T. The sign change of Γ_B together with its critical enhancement just above B_s and the approximate $1/B$ reduction with increasing distance from B_s are clear signatures of quantum-critical behaviour.^{45,44} Figure 12b exhibits Γ_B as a function of temperature at constant magnetic fields of $B = 8.45 \text{ T}$ and 8.55 T and at $B = 9 \text{ T}$. For the data taken at 8.45 T and 8.55 T we find the same $1/T$ dependence for $0.25 \text{ K} \leq T \leq 0.9 \text{ K}$ and a sign change in Γ_B indicating the proximity of a QCP. Similar to the observations for the AFHC compound CuP, the deviations of Γ_B from the ideal behaviour, as revealed in the experimental data at low temperatures, are assigned to the opening of a gap in the magnetic excitation spectrum. The gap has a size of $\Delta/k_B \sim 0.23 \text{ K}$ as determined by inelastic neutron-scattering experiments.¹¹⁰ At $B = 9 \text{ T}$, i.e., above the QCP, the temperature dependence of Γ_B is qualitatively different from the behaviour observed around the QCP. There is no sign change in Γ_B and the experimental data exhibit a $1/T$ dependence only for temperatures above 0.7 K as shown in Fig. 12b. The gap in the magnetic excitation spectrum is clearly visible through the strong reduction of Γ_B below 0.2 K.

Apart from the effects of a small excitation gap, the observed strongly enhanced Γ_B values of Cs_2CuCl_4 , indicating large absolute variations of entropy around the QCP, suggest an improved cooling performance of this frustrated quantum-spin system.

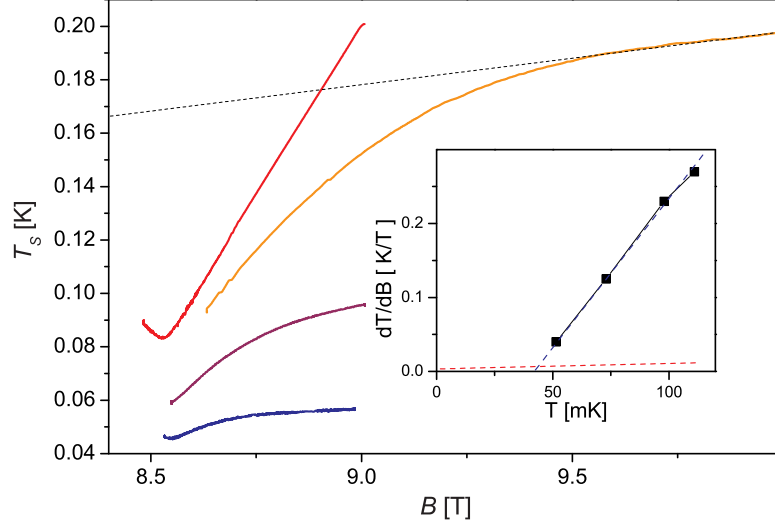


Fig. 13. Experimentally determined cooling curves for single crystalline Cs_2CuCl_4 obtained by demagnetizing the samples ($B \parallel a$ -axis) under almost adiabatic conditions. The starting temperature was $T_i = 0.2\text{ K}$ while cooling was performed from an initial field B_i of 9 T (red curve) and 10 T (orange curve). For comparison lowest-temperature cooling curves (violet and blue curves) are shown for $B_i = 9\text{ T}$ and $T_i < 0.1\text{ K}$. The dotted black line corresponds to the cooling curves of a paramagnet with the same initial parameters. Inset: cooling rate dT/dB of Cs_2CuCl_4 at a field of 8.65 T at various temperatures (black squares), as derived from the slopes of the various cooling curves at this field level, compared to that of a paramagnet (red circles) indicating the enhanced cooling performance in the quantum-critical regime.

Figure 13 shows a selection of cooling curves for Cs_2CuCl_4 in a limited $B - T$ parameter range and compares the cooling characteristics with that of a paramagnet. The four cooling curves for Cs_2CuCl_4 are obtained with different combinations of starting parameters T_i and B_i all of which are located close to the QCP. As can be seen in the main panel of Fig. 13 a final temperature $T_f = 0.083\text{ K}$ is reached with a starting temperature $T_i = 0.2\text{ K}$ and an initial field of $B_i = 9\text{ T}$. According to Fig. 12a, this combination of parameter corresponds to a magnetic Grüneisen parameter $\Gamma_B \approx 1\text{ T}^{-1}$ for Cs_2CuCl_4 . The average cooling rate dT/dB of this curve is approximately 0.25 K/T . For comparison, a paramagnet demagnetized from the same initial parameters would only reach a final temperature of $T_f = 0.19\text{ K}$, corresponding to a cooling rate $dT/dB = 0.02\text{ K/T}$. Even with $T_i = 0.2\text{ K}$ and $B_i = 0.5\text{ T}$, initial parameters much more suitable for paramagnets, T_f will stay slightly above 0.1 K . This is a further experimental proof of the enhanced cooling performance of a frustrated quantum-critical system. However, a slight variation of starting parameters to regions in the $B - T$ phase diagram, where Γ_B is no longer critically enhanced, the cooling performance of Cs_2CuCl_4 is significantly altered and the cooling rate becomes that of a simple paramagnet. For example, by keeping $T_i = 0.2\text{ K}$ and increasing B_i to fields above 9.5 T , the cooling curve of Cs_2CuCl_4 (orange

curve in Fig. 13) becomes identical to that expected for a paramagnet (black broken line). Also a reduced cooling rate is found by keeping B_i at 9 T while decreasing T_i to 0.096 K and 0.057 K. For the latter starting temperature, the high-field cooling behaviour around 9 T also matches that of a paramagnet. These experimental findings demonstrate that an enhanced cooling rate for Cs_2CuCl_4 is confined to its quantum-critical regime, whereas outside this regime on the high-field side, a performance identical to that of a paramagnet is revealed. Another way of visualizing this crossover in the cooling behaviour is provided by following the slopes of the various cooling curves at a constant field of 8.6 T, i.e., about 0.1 T above the critical field B_s , cf. inset of Fig. 13. At this field the cooling curves are, to a good approximation, linear in B , albeit with distinctly different slopes. As shown in the inset of Fig. 13, the cooling rate dT/dB of Cs_2CuCl_4 at $B = 8.65$ T (filled black squares) decreases linearly with temperature and crosses dT/dB of the paramagnet (filled red spheres) at around 40 mK for this field value.

(ii) Heavy-fermion intermetallics

Heavy-fermion systems are intermetallic compounds, mostly based on Ce, Yb, or U, where the $4f$ or $5f$ elements form a dense Kondo lattice. The physical properties of these materials are determined by strong electronic correlations and their ground state depends sensitively on the balance between the on-site Kondo screening and inter-site magnetic exchange coupling. In many heavy-fermion compounds quantum-critical behaviour has been observed and intensively investigated using thermodynamic methods.^{114,51} The MCE has been investigated down to lowest temperatures in the prototypical heavy-fermion metal YbRh_2Si_2 .⁵⁰ This system exhibits a field-tuned QCP which is related to the suppression of an antiferromagnetic order at a small critical field of $B_c = 0.06$ T. From magnetization measurements and specific heat data the magnetic Grüneisen parameter Γ_B was determined for YbRh_2Si_2 . As expected by theory Γ_B strongly increases around the QCP, a property which makes such heavy-fermion materials potential candidates for low-temperature magnetic cooling. Compared to the quantum-critical magnetic insulators, heavy-fermion metals may have a higher thermal conductivity at low temperatures, which can be of relevance for applications at temperatures significantly below 0.1 K.

Figure 14 shows the direct determination of the MCE for the heavy-fermion material $\text{Yb}(\text{Rh}_{0.95}\text{Fe}_{0.05})_2\text{Si}_2$ (open circles) using a newly developed method described in detail in Ref.¹¹⁵. The figure also displays the calculated values of the MCE based on magnetization and specific heat data (full squares). The experiment was performed above the QCP at the critical field of 0.05 T. As displayed in this figure Γ_B tends to diverge upon approaching the QCP, reaching a value of about 6 T^{-1} at 60 mK. Similar values of Γ_B are also found in the undoped material YbRh_2Si_2 .⁵⁰

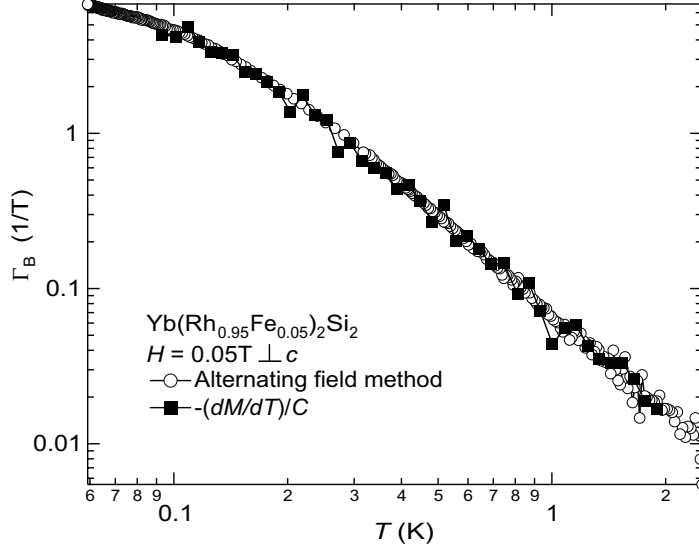


Fig. 14. Magnetic Grüneisen parameter Γ_B for the heavy-fermion material $\text{Yb}(\text{Rh}_{0.95}\text{Fe}_{0.05})_2\text{Si}_2$ as a function of temperature data taken from Ref. ¹¹⁵. The solid squares are calculated from magnetization and specific heat data whereas the open circles are the results of a direct determination of the MCE using an alternating field technique.

3.4. Cooling in ultracold gases

For noninteracting Fermi gases, the lowest reported temperatures, achieved in ^6Li samples by sympathetic evaporative cooling with bosonic ^{23}Na , are $T = 0.05 T_F = 93 \text{ nK}$ ¹¹⁶, while for a noninteracting BEC of ^{23}Na the Picokelvin regime has been reached by pure evaporative cooling, with a final temperature of $T \approx 500 \text{ pK}$. ¹¹⁷ For the weakly interacting regime (in a harmonic trap, before transfer into an optical lattice) that is relevant for lattice experiments, $0.13T/T_F$ ⁴³ and $0.3T/T_c$ ¹¹⁸ are the lowest reported *relative* temperatures for ultracold fermions and bosons, respectively, which correspond to $S/N \approx 1k_B$ and $S/N \approx 0.1k_B$ for an ideal gas. ⁷⁶ By using the spin-gradient demagnetization cooling technique in an optical lattice, isolated hyperfine spin distributions at positive and negative effective spin temperatures of 50 pK have been prepared. In the same experiment, the spin subsystem has also been used for cooling other (e.g., motional) degrees of freedom, leading to an equilibrated Mott insulator of ^{87}Rb atoms at approximately 350 pK . These temperatures are the lowest ones ever measured in any thermodynamic system so far. ⁸³

4. Applications

Nowadays magnetic refrigeration to temperatures below 100 mK is a well-established (even though not frequently used) cooling technology for those applications where low costs, low complexity and the ease of operation, combined with high reliability,

are in demand.

However, an important field of application for magnetic cryocoolers are space missions which, in turn, have driven an active development of this technology. In the primary focus are astronomy missions where low-temperature detectors and cooled telescopes are used. These applications require coolers which ensure long hold times for a given, fixed temperature below 100 mK. Furthermore the coolers can also support research in areas such as fundamental physics under microgravity. There is an increasing demand for magnetic coolers in space applications and therefore new developments have greatly expand their capabilities and range of use. An important step are multi-stage coolers with the ability to release heat at temperatures that can be provided by mechanical cryocoolers used as precooling stages. This makes it possible to operate the systems without the complexity of using liquid cryogens that heretofore have limited the mission lifetimes to 1-3 years.

4.1. Solid state systems

As described in the previous sections, the cooling performance of a given material is determined by the low-energy sector of its magnetic excitation spectrum, reflected in the entropy landscape as a function of B and T . For paramagnetic materials the residual interactions of the magnetic ions lead to a reduced entropy and eventually to long-range magnetic order at low temperatures. Diluting the paramagnetic systems by the partial substitution of the magnetic ions or by the incorporation of water into the crystal structure can suppress T_c . However, these modifications also reduce the density of magnetic ions, and by this, reduce the materials' cooling capacity per unit volume which is the amount of heat absorbed by the magnetic coolant (ΔQ_c in table 1). The crucial parameters, relevant in the selection of a suitable paramagnetic refrigerant for a given application, are the size of the spin s of the magnetic centres, the magnetic ion density and the material's ordering temperature T_c . The latter quantity eventually determines the material's operating range. Thus the goal is to use a material with T_c close to, but below, the desired operating temperature. For applications significantly below 100 mK, materials necessarily have to have a low spin value and a low ion density, which result in relatively low cooling capacity.

The use of quantum-critical materials, as a new concept for magnetic cooling, offers the possibility to get around some of the limitations of paramagnets. Quantum-critical systems, which per se lack long-range order, allow for large ion densities and thus afford large cooling capacities down to (in principle) arbitrarily low temperatures. In table 1 the paramagnetic standard materials for magnetic cooling below 100 mK and their relevant characteristics are listed together with the corresponding figures of quantum-critical systems. The spin-3/2 (CPA) and 5/2 (FAA) are the magnetic coolants for space applications^{9,10} whereas CMN with the lowest transition temperature is only used for cooling in laboratories or as a thermometer for low-temperature applications. An important quantity, especially for space applications, is the heat of magnetization ΔQ_m which has to be released to some

Table 1. Material properties, including the spin s , the ion density, and the magnetic ordering temperature T_c , and some performance characteristics for the state-of-the-art paramagnets ferric ammonium alum $\text{Fe}(\text{NH}_4)(\text{SO}_4)_2 \cdot 12\text{H}_2\text{O}$ (FAA) chromic potassium alum $\text{CrK}(\text{SO}_4)_2 \cdot 12\text{H}_2\text{O}$ (CPA), and cerium magnesium nitrate (CMN) in comparison with quantum-critical systems, including the antiferromagnetic spin-1/2 Heisenberg chain compound CuP and the frustrated quasi-2D triangular lattice antiferromagnet Cs_2CuCl_4 . ΔQ_m denotes the heat of magnetization which has to be released to some precooling stage, and ΔQ_c the heat the material is able to absorb after adiabatic demagnetization, see also Fig. 15. $\Delta Q_c/\Delta Q_m$ is the efficiency factor.

	CMN	CPA	FAA	CuP	Cs_2CuCl_4
spin s	1/2	3/2	5/2	1/2	1/2
ion density [cm^{-3}]	$1.05 \cdot 10^{21}$	$2.14 \cdot 10^{21}$	$2.15 \cdot 10^{21}$	$2.96 \cdot 10^{21}$	$4.32 \cdot 10^{21}$
T_c [K]	0.002	0.009	0.026	- ^a	- ^a
ΔQ_m [mJ/cm ³]		37.0	50.7	14.5	8.4
ΔQ_c [mJ/cm ³]		3.9	4.3	3.7	4.8
$\Delta Q_c/\Delta Q_m$		0.11	0.09	0.26	0.57

^a used for cooling above B_c .

precooling stage. Another item, quantifying the cooling performance, is ΔQ_c , the heat the material is able to absorb after adiabatic demagnetization, see also Fig. 15. $\Delta Q_c/\Delta Q_m$ is the efficiency factor. The data of ΔQ_m and ΔQ_c are calculated from the magnetization and cooling process shown in Fig. 15.

Table 1 compiles material properties, including the spin s , the ion density, and the magnetic ordering temperature T_c , and some performance characteristics for the state-of-the-art paramagnetic coolants ferric ammonium alum $\text{Fe}(\text{NH}_4)(\text{SO}_4)_2 \cdot 12\text{H}_2\text{O}$ (FAA),⁹⁶ chromic potassium alum $\text{CrK}(\text{SO}_4)_2 \cdot 12\text{H}_2\text{O}$ (CPA),⁹⁷ and cerium magnesium nitrate (CMN).⁹⁸ These figures are compared with those of quantum-critical systems, including the antiferromagnetic spin-1/2 Heisenberg chain compound CuP (1D AFHC) and Cs_2CuCl_4 (2D AFM) exhibit significantly higher ion densities; for Cs_2CuCl_4 , the ion density is a factor of about two larger compared to that of the paramagnets. Although the quantum-critical materials are $s = 1/2$ compounds, they exhibit a similar or even higher cooling capability ΔQ_c compared to the standard paramagnets. The main advantage provided by the quantum-critical systems is the amount of heat released to the high-temperature bath (precooling stage) ΔQ_m . For the process shown in Fig. 15, which assumes a bath temperature of 1.3 K, these values are significantly

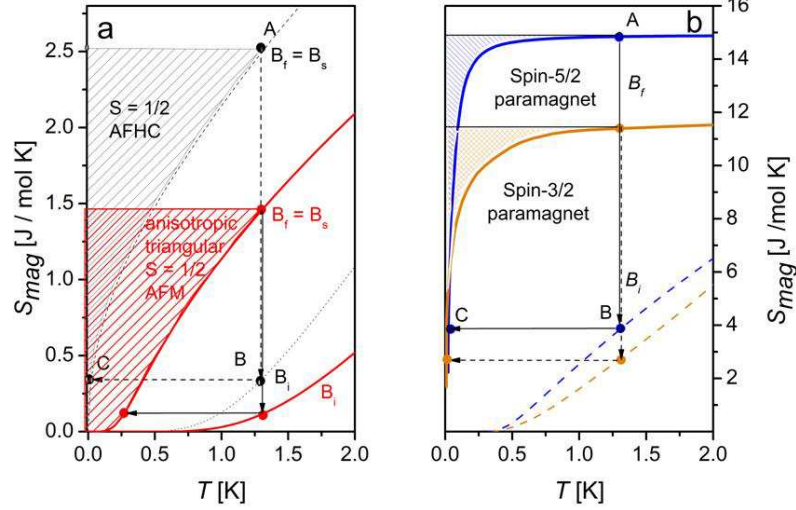


Fig. 15. (a) Molar magnetic entropy $S_{\text{mag}}(T, B = \text{const.})$ vs. T calculated for the spin-1/2 antiferromagnetic Heisenberg chain ($s = 1/2$ AFHC) with $J/k_B = 3.2$ K for an initial field of $B_i = 7.14$ T (broken grey line) and a final field $B_f = B_s = 4.09$ T (dotted grey line). The path AB denotes an isothermal magnetization process at $T_i = 1.3$ K, a realistic temperature for applications where precooling is provided by a pumped ^4He bath, followed by an adiabatic demagnetization (path BC). While the heat of magnetization, ΔQ_m , corresponds to the area of the rectangle $AB \times BC$, the amount of heat that the material is able to absorb, ΔQ_c , is given by the hatched area, cf. eq. 20 below. For comparison, the figure includes $S_{\text{mag}}(T, B = \text{const.})$ calculated for the frustrated two-dimensional triangular lattice spin-1/2 Heisenberg antiferromagnet with parameters appropriate for Cs_2CuCl_4 . (b) $S_{\text{mag}}(T, B = \text{const.})$ of the spin-5/2 paramagnetic salt $\text{Fe}(\text{NH}_4)(\text{SO}_4)_2 \cdot 12\text{H}_2\text{O}$ for $B_i = 2$ T (blue broken line) and $B_f = 0$ (blue solid line) and the spin-3/2 paramagnetic salt $\text{CrK}_4(\text{SO}_4)_2 \cdot 12\text{H}_2\text{O}$ for $B_i = 2$ T (orange broken line) and $B_f = 0$ (orange solid line). The data are taken from ^{119,99}. Panel (a) are taken from Ref. ⁶⁶.

smaller for the quantum-critical materials compared to the paramagnets. As a consequence, the efficiency $\Delta Q_c/\Delta Q_m$ of the cooling process for the quantum-critical systems largely exceeds the corresponding values for the paramagnets. This aspect can be of crucial importance for space applications. Given a limited capacity of the higher-temperature bath in these space missions, the higher efficiency of the cooling process directly leads to a significantly increase in the life time of the experiment.

Representative parameters characterizing the performance of a magnetic cryocooler include (i) the operating range, in particular the lowest temperatures T_f which can be obtained, (ii) the “hold time” of the coolant, which is inversely proportional to its cooling power and (iii) the efficiency $\Delta Q_c/\Delta Q_m$. The latter quantity can be read off the entropy-temperature diagram.

Figure 15 compiles curves of the molar magnetic entropy $S_{\text{mag}}(T, B = \text{const.})$ vs. T for the various materials discussed here and listed in Table 1. This includes calculations for the spin-1/2 antiferromagnetic Heisenberg chain with $J/k_B = 3.2$ K at an initial field $B_i = 7.14$ T (broken line) and a final field $B_f = B_s = 4.09$ T (dot-

ted line). The path AB denotes an isothermal magnetization process followed by an adiabatic demagnetization (path BC) down to the final temperature of approximately 24 mK. The heat of magnetization, ΔQ_m , produced by magnetizing the material at the initial temperature T_i , corresponds to the area of the rectangle AB \times BC, whereas the heat ΔQ_c the material can absorb after demagnetization to the final field B_f

$$\Delta Q_c = \int_{T_f}^{T_i} T \left(\frac{\partial S}{\partial T} \right)_{B_f} dT \quad (20)$$

is given by the hatched area. The efficiency $\Delta Q_c/\Delta Q_m$ in the temperature range indicated amounts to 26% for the spin-1/2 antiferromagnetic Heisenberg chain. For comparison, we show in Fig. 15 $S_{\text{mag}}(T, B = \text{const.})$ calculated for the anisotropic version of the two-dimensional triangular-lattice spin-1/2 Heisenberg antiferromagnet with $J/k_B = 3J'/k_B = 4.3$ K, at $B_i = 12.0$ T and $B_f = B_s = 8.55$ T, i.e., parameters appropriate for Cs_2CuCl_4 ^b. For this strongly frustrated system and the temperature range indicated an efficiency $\Delta Q_c/\Delta Q_m$ as high as about 57% is obtained.

These numbers for the quantum-critical systems can be compared with that of the spin-5/2 paramagnetic salt $\text{Fe}(\text{NH}_4)(\text{SO}_4)_2 \cdot 12\text{H}_2\text{O}$ (FAA). Figure 15 shows $S_{\text{mag}}(T, B = \text{const.})$ for $B_i = 2$ T (blue broken line) and $B_f = 0$ (blue solid line) corresponding to $T_i = 1.3$ K and $T_f = 22$ mK. We find $\Delta Q_m = 50.71$ mJ/cm³ and $\Delta Q_c = 4.33$ mJ/cm³ which corresponds to an efficiency $\Delta Q_c/\Delta Q_m$ of only 9%. In a similar procedure we obtained for the spin-3/2 paramagnet $\text{CrK}(\text{SO}_4)_2 \cdot 12\text{H}_2\text{O}$ (CPA) $\Delta Q_m = 39.02$ mJ/cm³ and $\Delta Q_c = 3.89$ mJ/cm³. This results in an efficiency factor $\Delta Q_c/\Delta Q_m$ of about 11%.

5. Perspectives

In this article we review recent developments in cooling technologies for condensed matter and cold gas experiments. The demand for new coolants in these areas arises from several factors which are different for both fields. For condensed matter systems, the reasons mainly lie in the restricted availability of Helium, especially ³He, and the need to optimize the cooling performance with regard to space, weight or the ease of operation. On the other hand, for ultracold gases, it is the desire for reaching low enough temperatures to eventually access solid state-type ordered states such as quantum magnetism or *d*-wave superfluidity.

The new approach discussed here is based on taking advantage of many-body interactions in the system to be cooled. We discuss some proof-of-principle demonstrations for cooling materials through quantum criticality and discuss the effects of geometric frustration. By comparing experimental results with theoretical calculations on model systems, we are able to identify limiting factors for the real systems

^b A chain mean-field theory turned out to be more appropriate in this case than a plain exact diagonalization as in section 3.1.3 for the isotropic triangular lattice. see Ref. ⁶⁶ for more details.

an indicate routes towards next generation many-body coolants. We demonstrate that these systems have the potential to outperform state-of-the-art conventional refrigerant materials.

For ultracold gases we have discussed two recent approaches towards adiabatic cooling of the many-body system, based on spin-gradient demagnetization and the Pomeranchuk effect, which directly take into account interparticle interactions in an optical lattice. Future developments along these directions will likely involve reduced spatial mass- and entropy-transport, in order to reduce non-adiabatic effects which limit cooling efficiency, and local addressing techniques such as the optical quantum gas microscope.

References

1. P. Debye, *Ann. Phys. Leipzig* **81**, 1154 (1926).
2. W. F. Giaque, *J. Amer. Chem. Soc.* **49**, 1864 (1927).
3. O. V. Lounasmaa, *Experimental Principles and Methods Below 1 K* (Academic Press, New York, 1974).
4. A. M. Tishin and I. Spichkin, *The Magnetocaloric Effect and its Applications* (Institute of Physics, Bristol, 2003).
5. K. A. Gschneidner, V. K. Pecharsky, and A. O Tsokol, *Rep. Prog. Phys.* **68**, 1479 (2005).
6. K. A. Gschneidner and V. K. Pecharsky, *Phys. Rev. Lett.* **78**, 4494 (1997).
7. E. Brück, *J. Phys. D: Appl. Phys.* **38**, R381 (2005).
8. O. Tegus *et al.*, *Nature* **415**, 150 (2002).
9. P. J. Shirron, *J. Low Temp. Phys.* **148**, 915 (2007).
10. C. Hagemann and P. L. Richards, *Cryogenics* **32**, 319 (1999).
11. Yu I. Spichkin, A. K. Zvezdin, S. P. Gubin, A. S. Mischenko, and A. M. Tishin, *J. Phys. D: Appl. Phys.* **34**, 1162 (2001).
12. R. Sessoli, *Angew. Chem. Int. Ed.* **51**, 43 (2012).
13. M. Evangelisti, F. Luis, L. J. De Jongh, and M. Affronte, *J. Mater. Chem.* **16**, 2534 (2006).
14. J. Schnack, R. Schmidt, and J. Richter, *Phys. Rev. B* **76**, 054413 (2007).
15. A. Honecker and M. E. Zhitomirsky, *J. Phys.: Conf. Ser.* **145**, 012082 (2009).
16. A. P. Ramirez, *Annu. Rev. Mater. Sci.* **24**, 453 (1994).
17. P. Schiffer and A. P. Ramirez, *Comments Condens. Matter Phys.* **18**, 21 (1996).
18. J. E. Greedan, *J. Mater. Chem.* **11**, 37 (2001).
19. R. Moessner, *Can. J. Phys.* **79**, 1283 (2001).
20. C. Lacroix, P. Mendels, and F. Mila (Eds.), *Introduction to Frustrated Magnetism, Springer Series in Solid-State Sciences* **164** (Springer, Berlin, 2011).
21. R. A. Fisher, G. E. Brodale, E. W. Hornung, and W. F. Giaque, *J. Chem. Phys.* **59**, 4652 (1973).
22. E. W. Hornung, R. A. Fisher, G. E. Brodale, and W. F. Giaque, *J. Chem. Phys.* **61**, 282 (1974).
23. G. E. Brodale, E. W. Hornung, R. A. Fisher, and W. F. Giaque, *J. Chem. Phys.* **62**, 4041 (1975).
24. J. A. Barclay and W. A. Steyert, *Cryogenics* **22**, 73 (1982).
25. J. Villain, *Z. Phys. B: Condens. Matter* **33**, 31 (1971).
26. M. E. Zhitomirsky, *Phys. Rev. B* **67**, 104421 (2003).

27. S. S. Sosin, L. A. Prozorova, A. I. Smirnov, A. I. Golov, I. B. Bertukov, O. A. Petrenko, G. Balakrishnan, and M. E. Zhitomirsky, *Phys. Rev. B* **71**, 094413 (2005).
28. J. Schnack, H.-J. Schmidt, J. Richter, and J. Schulenburg, *Eur. Phys. J. B*, **24**, 475 (2001).
29. J. Schulenburg, A. Honecker, J. Schnack, J. Richter, and H.-J. Schmidt, *Phys. Rev. Lett.* **88**, 167207 (2002).
30. M. E. Zhitomirsky and A. Honecker *J. Stat. Mech.: Theor. Exp.*, P07012 (2004).
31. M. E. Zhitomirsky and H. Tsunetsugu, *Phys. Rev. B* **70**, 100403(R) (2004).
32. M. E. Zhitomirsky and H. Tsunetsugu, *Prog. Theor. Phys. Supplement* **160**, 361 (2005).
33. O. Derzhko, J. Richter, A. Honecker, and H.-J. Schmidt, *Fizika Nizkikh Temperatur (Kharkiv)* **33**, 982 (2007) [*Low Temp. Phys.* **33**, 745 (2007)].
34. E. Ambler and R. P. Hudson, *Rep. Prog. Phys.* **18**, 251 (1955).
35. V. K. Pecharsky and K. A. Gschneidner, *J. Mag. Mag. Mat.* **200**, 44 (1999).
36. W. Hofstetter, J. I. Cirac, P. Zoller, E. Demler, and M. D. Lukin, *Phys. Rev. Lett.* **89**, 220407 (2002).
37. I. Bloch, J. Dalibard, and W. Zwerger, *Rev. Mod. Phys.* **80**, 885 (2008).
38. R. Jördens *et al.*, *Nature* **455**, 204(2008).
39. U. Schneider *et al.*, *Science* **322**, 1520 (2008).
40. D. Greif, T. Uehlinger, G. Jotzu, L. Tarruell, and T. Esslinger, *Science* **340**, 1307 (2013).
41. S. Trotzky *et al.*, *Science* **319**, 295 (2008).
42. J. Simon, W. S. Bakr, R. Ma, M. E. Tai, P. M. Preiss, and M. Greiner, *Nature* **472**, 307 (2011).
43. R. Jördens *et al.*, *Phys. Rev. Lett.* **104**, 180401 (2010).
44. L. Zhu, M. Garst, A. Rosch, and Q. Si, *Phys. Rev. Lett.* **91**, 066404 (2003).
45. M. Garst and A. Rosch, *Phys. Rev. B* **72**, 205129 (2005).
46. I. Kimura and N. Uryû, *J. Phys. Soc. Jpn.* **23**, 1204 (1967).
47. P. Camus, G. Vermeulen, A. Volpe, S. Triqueneaux, A. Benoit, J. Butterworth, S. d'Esquivan, and T. Tirolien, *J. Low Temp. Phys.* **176**, 1069 (2014).
48. S. Sachdev, *Quantum Phase Transitions*, 2nd Edition (Cambridge University Press, 2011).
49. M. Vojta, *Rep. Prog. Phys.* **66**, 2069 (2003).
50. Y. Tokiwa, T. Radu, C. Geibel, F. Steglich, and P. Gegenwart, *Phys. Rev. Lett.* **102**, 066401 (2009).
51. P. Gegenwart, Y. Tokiwa, J. G. Donath, R. Kuchler, C. Bergmann, H. S. Jeevan, E. D. Bauer, J. L. Sarrao, C. Geibel, and F. Steglich, *J. Low Temp. Phys.* **161**, 117 (2010).
52. B. Wolf *et al.*, *Proc. Nat. Acad. Sci., USA*, **108**, 6862 (2011).
53. J. C. Bonner and J. F. Nagle, *Phys. Rev. A* **5**, 2293 (1972).
54. C. Trippé, A. Honecker, A. Klümper, and V. Ohanyan, *Phys. Rev. B* **81**, 054402 (2010).
55. R. B. Griffiths, *Phys. Rev.* **133**, A768 (1964).
56. J. C. Bonner and M. E. Fisher, *Proc. Phys. Soc.* **80**, 508 (1962).
57. J. C. Bonner, *Numerical Studies on the Linear Ising-Heisenberg Model*, Ph.D. thesis (University of London, 1968).
58. J. C. Bonner and J. D. Johnston, *Physica* **86-88B**, 653 (1977).
59. K. Amaya, Y. Tokunaga, R. Yamada, Y. Ajiro, and T. Haseda, *Phys. Lett. A* **28**, 732 (1969).
60. M. W. van Tol, K. M. Diederix, and N. J. Poulis, *Physica* **64**, 363 (1973).

61. M. Tachiki and T. Yamada, *J. Phys. Soc. Jpn.* **28**, 1413 (1970).
62. M. Tachiki, T. Yamada, and S. Maekawa, *J. Phys. Soc. Jpn.* **29**, 663 (1970).
63. K. M. Diederix, H. W. J. Blöte, J. P. Groen, T. O. Klaassen, and N. J. Poulis, *Phys. Rev. B* **19**, 420 (1979).
64. D. A. Tennant, B. Lake, A. J. A. James, F. H. L. Essler, S. Notbohm, H.-J. Mikeska, J. Fielden, P. Kögerler, P. C. Canfield, and M. T. F. Telling, *Phys. Rev. B* **85**, 014402 (2012).
65. B. Willenberg, H. Ryll, K. Kiefer, D. A. Tennant, F. Groitl, K. Rolfs, P. Manuel, D. Khalyavin, K. C. Rule, A. U. B. Wolter, and S. Süllow, *Phys. Rev. B* **91**, 060407(R) (2015).
66. M. Lang, B. Wolf, A. Honecker, L. Balents, U. Tutsch, P. T. Cong, G. Hofmann, N. Krüger, F. Ritter, W. Assmus, and A. Prokofiev, *Phys. Status Solidi B* **250**, 457 (2013).
67. A. Honecker and S. Wessel, *Physica B* **378-380**, 1098 (2006).
68. D. Jaksch, C. Bruder, J. I. Cirac, C. W. Gardiner, and P. Zoller, *Phys. Rev. Lett.* **81**, 3108 (1998).
69. P. Soltan-Panahi, J. Struck, P. Hauke, A. Bick, W. Plenkers, G. Meineke, C. Becker, P. Windpassinger, M. Lewenstein and K. Sengstock, *Nature Phys.* **7**, 434 (2011).
70. G.-B. Jo, J. Guzman, C. K. Thomas, P. Hosur, A. Vishwanath, and D. M. Stamper-Kurn, *Phys. Rev. Lett.* **108**, 045305 (2012).
71. J. F. Sherson, C. Weitenberg, M. Endres, M. Cheneau, I. Bloch, and S. Kuhr, *Nature* **467**, 68 (2010); W. S. Bakr, J. I. Gillen, A. Peng, S. Fölling, and M. Greiner, *Nature* **462**, 74 (2009).
72. T. Fukuhara, P. Schauß, M. Endres, S. Hild, M. Cheneau, I. Bloch, and C. Gross, *Nature* **502**, 76 (2013).
73. L. M. Duan, E. Demler, and M. D. Lukin, *Phys. Rev. Lett.* **91**, 090402 (2003).
74. E. Altman, W. Hofstetter, E. Demler, and M. D. Lukin, *New J. Phys.* **5**, 113 (2003).
75. A. Hubener, M. Snoek, and W. Hofstetter, *Phys. Rev. B* **80**, 245109 (2009).
76. D. C. McKay and B. DeMarco, *Rep. Prog. Phys.* **74**, 054401 (2011).
77. F. Werner, O. Parcollet, A. Georges, and S. R. Hassan, *Phys. Rev. Lett.* **95**, 056401 (2005).
78. B. Capogrosso-Sansone, Ş. G. Söyler, N. V. Prokof'ev, and B. V. Svistunov, *Phys. Rev. A* **81**, 053622 (2010).
79. B. Schmidt, M. R. Bakhtiari, I. Titvinidze, U. Schneider, M. Snoek, and W. Hofstetter, *Phys. Rev. Lett.* **110**, 075302 (2013).
80. M. Lubasch, V. Murg, U. Schneider, J. I. Cirac, and M. C. Banuls, *Phys. Rev. Lett.* **107**, 165301 (2011).
81. M. Fattori, T. Koch, S. Goetz, A. Griesmaier, S. Hensler, J. Stuhler, and T. Pfau, *Nature Phys.* **2**, 765 (2006).
82. D. M. Weld, P. Medley, H. Miyake, D. Hucul, D. E. Pritchard, and W. Ketterle, *Phys. Rev. Lett.* **103**, 245301 (2009).
83. P. Medley, D. M. Weld, H. Miyake, D. E. Pritchard, and W. Ketterle, *Phys. Rev. Lett.* **106**, 195301 (2011).
84. Y. Li, M. R. Bakhtiari, L. He, and W. Hofstetter, *Phys. Rev. A* **85**, 023624 (2012).
85. Y. Li, M. R. Bakhtiari, L. He, and W. Hofstetter, *Phys. Rev. B* **84**, 144411 (2011).
86. K. Byczuk and D. Vollhardt, *Phys. Rev. B* **77**, 235106 (2008).
87. W. J. Hu, and N. H. Tong, *Phys. Rev. B* **80**, 245110 (2009).
88. P. Anders, E. Gull, L. Pollet, M. Troyer, and P. Werner, *Phys. Rev. Lett.* **105**, 096402 (2010).
89. M. Snoek and W. Hofstetter, Chapter in *Quantum Gases: Finite Temperature and Non-Equilibrium Dynamics*, (Vol. 1 Cold Atoms Series), N. P. Proukakis, S. A. Gar-

- diner, M. J. Davis and M. H. Szymanska, eds. (Imperial College Press, London, 2013); see also arXiv:1007.5223.
90. D. M. Weld, H. Miyake, P. Medley, D. E. Pritchard, and W. Ketterle, *Phys. Rev. A* **82**, 051603 (2010).
91. A. Sotnikov, D. Cocks, and W. Hofstetter, *Phys. Rev. Lett.* **109**, 065301 (2012).
92. A. Sotnikov, M. Snoek, and W. Hofstetter, *Phys. Rev. A* **87**, 053602 (2013).
93. S. Fuchs, E. Gull, L. Pollet, E. Burovski, E. Kozik, T. Pruschke, and M. Troyer, *Phys. Rev. Lett.* **106**, 030401 (2011).
94. S. Taie, R. Yamazaki, S. Sugawa, and Y. Takahashi, *Nature Phys.* **8**, 825 (2012).
95. M. Colomé-Tatché, C. Klempt, L. Santos, and T. Vekua, *New J. Phys.* **13**, 113021 (2011).
96. A. H. Cooke, *Proc. Roy. Soc. A* **62**, 269 (1949).
97. B. Bleaney, *Proc. Roy. Soc. A* **204**, 203 (1950).
98. A. H. Cooke, H. J. Duffus, and W. P. Wolf, *Philos. Mag.* **44**, 623 (1953).
99. F. Pobell, *Matter and Methods at Low Temperature* (Springer, Berlin, 1992).
100. G. W. Wilson and P. T. Timbie, *Cryogenics* **39**, 303 (1995).
101. R. M. Mueller, Chr. Buchal, H. R. Folle, M. Kubota, and F. Pobell, *Cryogenics* **20**, 395 (1980).
102. I. D. Hepburn, I. Davenport, and A. Smith, *Space Science Reviews* **74**, 215 (1995).
103. P. R. Hammar, M. B. Stone, D. H. Reich, C. Broholm, P. J. Gibson, M. M. Turnbull, C. P. Landee, and M. Oshikawa, *Phys. Rev. B* **59**, 1008 (1999).
104. B. Lake, D. A. Tennant, C. D. Frost, and S. E. Nagler, *Nature Mater.* **4**, 329 (2005).
105. F. M. Woodward, P. J. Gibson, G. B. Jameson, C. P. Landee, M. M. Turnbull, and R. D. Willett, *Inorg. Chem.* **46**, 4256 (2007).
106. O. Castillo, A. Lague, J. Sertucha, P. Román, F. Lloret, *Inorg. Chem.* **39**, 6142 (2000).
107. A. Klümper, *Eur. Phys. J B* **5**, 677 (1998).
108. A. V. Prokofiev, W. Assmus, K. Removič-Langer, P. Pashchenko, Y. Tsui, B. Wolf, and M. Lang, *Cryst. Res. Technol.* **42**, 394 (2007).
109. R. Tarasenko, E. Čížmár, A. Orendáčová, J. Kuchár, J. Černák, J. Prokleška, V. Sechovský, and M. Orendáč, *Solid State Sciences* **28**, 14 (2014).
110. R. Coldea *et al.*, *J. Phys. Condens. Matter* **8**, 7473 (1996).
111. R. Coldea *et al.*, *Phys. Rev. Lett.* **88**, 137203 (2002).
112. R. Coldea *et al.*, *Phys. Rev. Lett.* **86**, 1335 (2001).
113. T. Radu, H. Wilhelm, V. Yushankhai, D. Kovrizhin, R. Coldea, Z. Tylczynski, T. Lühmann, and F. Steglich, *Phys. Rev. Lett.* **95**, 127202 (2005).
114. P. Gegenwart, Q. Si, and F. Steglich, *Nature Phys.* **4**, 186 (2008).
115. Y. Tokiwa and P. Gegenwart, *Rev. Sci. Instr.* **82**, 013905 (2011).
116. Z. Hadzibabic, S. Gupta, C. A. Stan, C. H. Schunck, M. W. Zwierlein, K. Dieckmann, and W. Ketterle, *Phys. Rev. Lett.* **91**, 160401 (2003).
117. A. E. Leanhardt, T. A. Pasquini, M. Saba, A. Schirotzek, Y. Shin, D. Kielpinski, D. Pritchard, and W. Ketterle, *Science* **301**, 1513 (2003).
118. D. McKay, M. White, M. Pasienski, and B. DeMarco, *Nature* **453**, 76 (2008).
119. O. E. Vilches and J. C. Wheatly, *Phys. Rev.* **148**, 509 (1966).